Department of Precision and Microsystems Engineering

Layer thickness control: Improving manufacturability in fabrication sequence optimization for multi-axis additive manufacturing

Mike Lansu

Report no	: 2023.072
Coach	: Ir. Kai Wu
Professor	: Dr. Jun wu, Prof. Dr. Ir. Fred van Keulen
Specialisation	: Computational Design and Mechanics
Type of report	: M.Sc Thesis
Date	: 28 September 2023

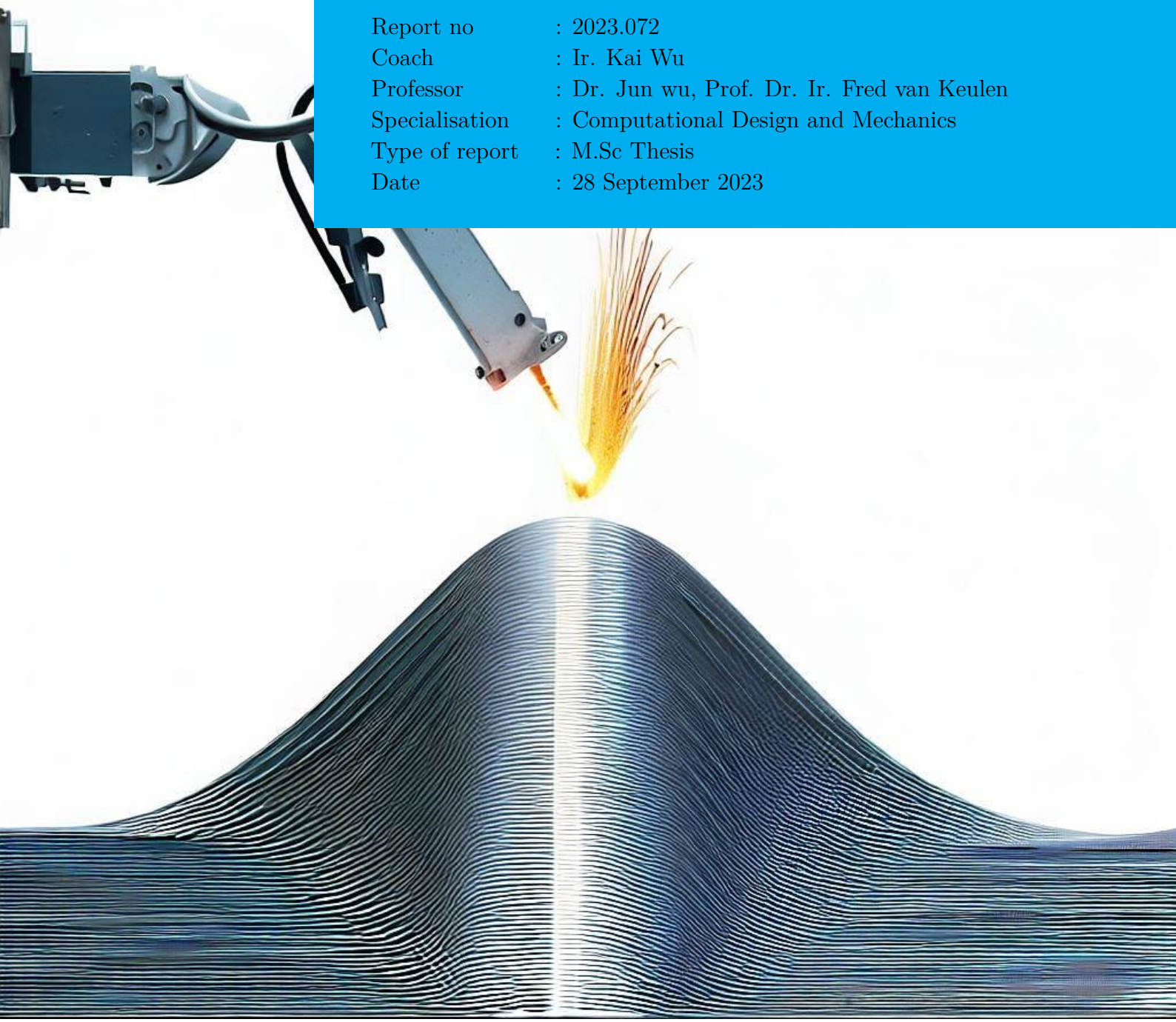

Layer thickness control

Improving manufacturability in fabrication sequence optimization for multi-axis additive manufacturing

by

Mike Lansu

Student Name	Student Number
Mike Lansu	4456092

Senior supervisor: Jun Wu
Fred van Keulen
Daily supervisor: Kai Wu
Project Duration: August, 2022 - September, 2023
Faculty: 3mE, Mechanical Engineering, TU Delft

Cover: AI (Dall-E) generated image of a welded normal distribution curve

TU Delft

Acknowledgements

I would like to express my appreciation to my supervisors Jun Wu and Kai Wu for their valuable help during this thesis project. You have provided me the freedom to find my way in solving this research puzzle and offered me great guidance where needed. I appreciate that very much. I would also like to thank Manabendra and Budhaditya. From the same moment, one year ago, we went through the same process and I have enjoyed the weekly meetings and moments we helped each other out.

Mike Lansu
Delft, September 2023

Abstract

The use of multi-axis additive manufacturing has enabled the possiblity to fabricate parts using curved layer deposition. Compared to the traditional deposition using planar layers of a fixed thickness, multi-axis additive manufacturing significantly increases the number of possible fabrication sequences. With the introduction of a time component for topology optimization in recent work, fabrication-process-dependent physics can now be incorporated in the optimization process. The fabrication sequence resulting from such complex optimizations can lead to layers with large variations in thickness. For manufacturability reasons, considering multi-axis additive manufacturing, this variation should be controlled. In this thesis, we present a method to control the variation in thickness of the projected layers to improve the manufacturability. We use the continuous pseudo-time field and its gradients to track the development of the layer boundaries. To demonstrate the effectiveness of the method, we apply the thickness control method on a fabrication sequence optimization for minimizing thermal distortion. The results show that the proposed method is able to reduce the variation of thicknesses compared to the original sequence optimization without thickness control resulting in improved manufacuturability.

Contents

Nomenclature

Abbreviations

Abbreviation	Definition
AM	Additive Manufacturing
CAD	Computer-Aided Design
FEM	Finite Element Method
LSC	Length Scale Control
MMA	Method of Moving Asymptotes
TO	Topology Optimization
SIMP	Solid Isotropic Material with Penalization
STTO	Space-Time Topology Optimization
WAAM	Wire Arc Additive Manufacturing

1

Introduction

Additive manufacturing (AM), commonly known as 3D printing, has emerged as a disruptive technology, revolutionizing various sectors including aerospace, automotive, healthcare, and consumer goods. With its layer-by-layer deposition of material, it provides a flexible production method suitable for fast prototyping. Additive manufacturing allows for the production of complex geometries that might be impossible or cost-prohibitive using traditional manufacturing methods. The use of multi-axis robotic systems in additive manufacturing has increased the manufacturing flexibility even further. Instead of the standard planar layer deposition, additive manufacturing along a curved surface is now a possibility.

In a recent study [32] a new type of optimization, called *Space-Time Topology Optimization* (STTO), was proposed. In this method the optimization is done concurrently on both the structural layout of the design and the fabrication sequence for additive manufacturing. The fabrication sequence can be derived from the psuedo-time field. The introduction of the time field into the optimization process offers the opportunity to optimize for process-dependent physics. Recent work [31] demonstrated the possibility of fabrication sequence optimization for minimizing distortion using such a pseudo-time field.

The addition of the time-field in the optimization process offers opportunities to optimize for complex fabrication-process-dependent physics problems. A limiting factor in optimizing the fabrication sequence of such problems is the manufacturability of the resulting sequence. Results show that the optimization for minimizing distortion leads to non-uniform layer thickness. While some additive manufacturing methods, such as Wire-Arc Additive Manufacturing (WAAM) can control the thickness of the deposition to some extend, the flexibility is rather limited. Depending on the WAAM equipment specifications, the thickness of a layer has a lower and an upper bound. Therefore, to make such designs feasible for fabrication these restrictions on layer thickness should be incorporated in the optimization process.

The aim for this thesis research is to propose a method to ensure manufacturability of fabrication sequence optimized designs. The optimization for minimizing distortion is chosen to validate the effectiveness of the method, but the proposed methods should not be limited to this specific optimization. To get a better understanding of the origin of the problem in this research, some background information is required. In this section an introduction is given on additive manufacturing and topology optimization.

1.1. Introduction to additive manufacturing

Additive manufacturing (AM), also known as 3D-printing is a computer controlled production method that can create three-dimensional objects by layer-by-layer deposition of material [34]. Compared to traditional fabrication techniques such as subtractive manufacturing (milling, turning, drilling), formative manufacturing (forging, rolling, extrusion) and molding and casting, AM offers various advantages. The direct deposition of the material can reduce the material waste and gives more design freedom than molding and casting [17]. Within AM several types exist which can be divided in groups depending on the material deposition method:

- **VAT Photopolymerisation** makes use of a liquid photopolymer resin. An ultraviolet light is used to cure the resin layer by layer to produce the part.
- **Blinder jetting** makes use of two materials deposited by a printing head in alternating layers. A powder based material is combined with the binder material to form the object.
- **Material extrusion** like Fused Deposition Modeling (FDM) draws thermoplastics through a heated nozzle to deposit layer by layer. The nozzle can move in multiple directions to create 3D objects.
- **Powder bed fusion** makes use of powder materials deposited layer by layer. The layer of powder is melted by electron beams or lasers to melt the material onto the substrate after which excess powder can be removed.
- **Directed Energy Deposition** makes use of a laser or arc to melt material onto the substrate.

These types of additive manufacturing each offer their advantages and disadvantages. Some AM techniques only work on a 3-axis machine and can only print planar layers. In Figure 1.1 the fabrication of a 3-axis FDM-printer is shown. This type of printer is mostly used to fabricate small light-weight parts by successively producing planar layers.

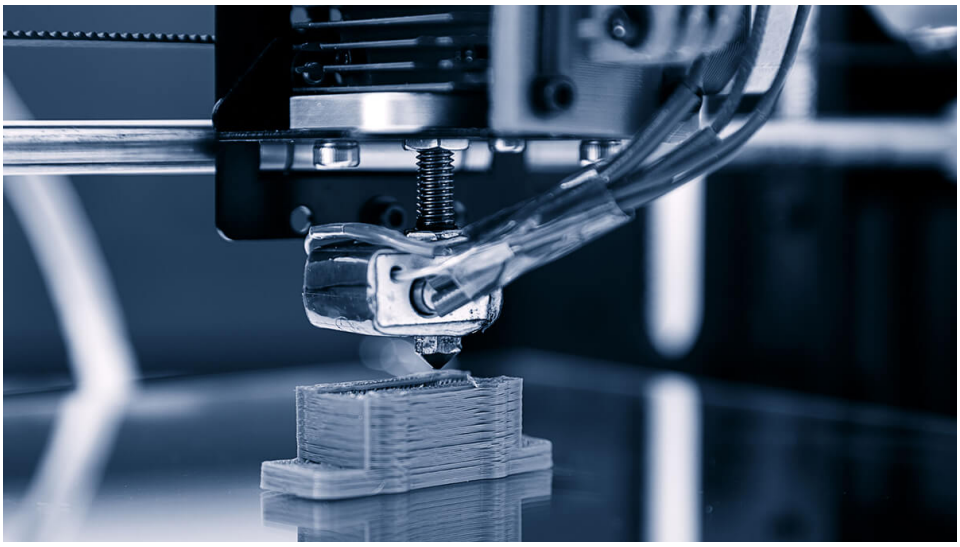

Figure 1.1: A 3-axis FDM-printer fabricating a part [28]

With the introduction of multi-axis additive manufacturing, the flexibility in manufacturing methods such as wire and arc additive manufacturing further increased. The multi-axis freedom allows to change the position as well as the angle of the printing nozzle or building plate, to deposit material along a curved surface. This prevents the so-called *staircase effect* when manufacturing parts with curved surfaces, resulting in a smoother surface finish and the possibility to print support-free parts.

1.1.1. Wire and Arc Additive Manufacturing

Wire and Arc Additive Manufacturing (WAAM) is a specific type of additive manufacturing that belongs to the *Direct Energy Deposition* (DED) group. The wire and arc refers to the welding process often used for joining metal parts. Attaching the welding torch to a multi-axis robotic arm enables melting the wire feedstock into 3D objects. WAAM can be used to produce both small and large-scale parts

without significant changes to the setup or process. This makes it adaptable to different production needs, from detailed components to large structural elements. WAAM can work with a wide range of metallic materials, including steel, aluminum, titanium, and nickel-based alloys [28]. This flexibility can enable a broad array of applications across various industries. Parts manufactured using WAAM often demonstrate good mechanical properties, comparable or sometimes even superior to those created using traditional manufacturing methods. This is particularly significant for industries where structural integrity is important, such as aerospace and automotive sectors. In Figure 1.2 a generic scheme is visualised of a multi-axis WAAM setup.

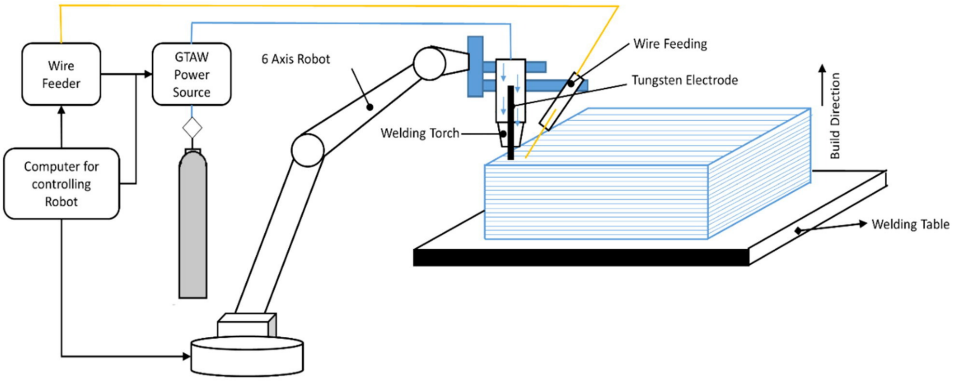

Figure 1.2: Generic scheme of the WAAM process [28]

The dimensions of a single welded layer have a minimum and maximum height that ranges approximately from 1-2 mm. The minimum bead thickness is determined by the minimum power required to weld the wire and the largest torch speed at which a stable weld bead is produced [10]. By controlling the power, the torch speed and the wire feed rate, the dimensions of the weld bead can be controlled [10] [20].

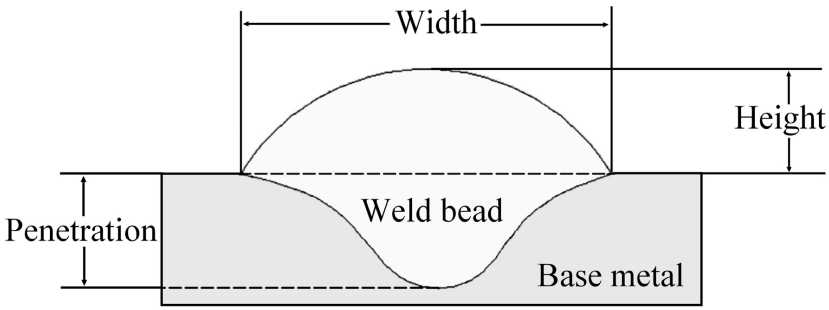

Figure 1.3: Dimensions of the weld bead [20]

While WAAM has good mechanical properties, it also has its downsides. WAAM generates large thermal gradients due to localized melting and solidification of material. These thermal gradients result in residual stresses within the part, leading to thermal distortions. These distortions are dependent on WAAM parameters and its fabrication sequence [23] and can lead to inaccurate shapes and dimensions when compared to the CAD-model it was based on. Another downside of WAAM is the high surface roughness. Due to the melt pool characteristics, the dimensions of the deposited weld bead can be hard to control which can result in a rough surface finish. To get to a desired surface finish, post-processing of the part is often required.

1.2. Integration of additive manufacturing with topology optimization

The fabrication flexibility of additive manufacturing equipment is best utilized with the often complex designs generated by topology optimization [38] [14] [36]. In this section we will first shortly explain what topology optimization is.

Topology optimization (TO) [22] is a structural optimization method that uses algorithmic models to optimize material layout within a user-defined space for a given set of loads, conditions, and constraints. The goal of the optimization is formulated in the objective function. This objective function reflects the performance of the design. By computing the derivatives of the objective function w.r.t. the design variable, such as the density, optimization algorithms such as the Method of Moving Asymptotes (MMA) [25] can steer the optimization to maximize the desired performance. This often results in very natural and non-intuitive shapes as can be seen in Figure 1.4.

Figure 1.4: Example of a part designed by topology optimization (*3Dprint.com*)

The integration of additive manufacturing with topology optimization offers significant advantages over conventional manufacturing techniques. AM enables the direct realization of optimized designs by building complex structures layer by layer, eliminating many of the constraints associated with traditional subtractive manufacturing processes. This integration allows engineers to exploit the full potential of topology optimization, translating optimized designs into physical prototypes or end-use components with unprecedented design freedom.

For many AM processes, support structures are needed to be able to manufacture parts with large overhangs. Such support structures require post-processing of the part and can lead to an increased weight of the part due to inaccessible support material. Support-free AM methods and overhang-free topology optimization [27] are being developed to solve this problem, as it still remains a challenge [14].

Additive manufacturing technologies, such as WAAM, offer the ability to produce intricate, highly customized geometries without the need for assembly or complex tooling. The layer-by-layer deposition process allows for the fabrication of complex internal features, lightweight lattice structures, and optimized material distributions that are often the outcome of topology optimized designs. By precisely controlling the material placement, WAAM techniques can replicate the optimized designs accurately, ensuring that the intended performance characteristics are realized in the final product. When using multi-axis WAAM, curved layer deposition becomes possible. This can reduce the need of support structures which will then reduce the need of post-processing of the parts.

1.3. Length-scale control issues associated with sequence optimization

The use of multi-axis additive manufacturing enables the fabrication of parts in an endless number of possible fabrication sequences. With challenges such as large overhangs in parts often requiring support structures, smart toolpath planning can result in improved part quality and a valuable reduction in post-processing. With the introduction of fabrication sequence optimization [31] the fabrication order can be optimized for process dependent physical problems, instead of slicing the part into planar layers

using conventional slicing algorithms. Fabrication sequence optimization can play a crucial role in ensuring the successful implementation of additive manufacturing (AM) processes. By determining the optimal order of manufacturing operations, the fabrication sequence optimization approach enables the production of complex geometries and customized components. However, one of the challenges that arise during fabrication sequence optimization for AM is managing the variations in layer thickness resulting from the optimization. The limited ability of AM equipment to deposit layers with varying thickness poses a significant constraint that must be carefully addressed to achieve manufacturable designs and the desired part quality and functionality.

Additive manufacturing equipment is typically designed to deposit uniform layers of material during the build process. The layer thickness is often predetermined and depends on the specific equipment and process parameters. Deviating from the predefined layer thickness introduces challenges in maintaining a consistent deposition rate and controlling the flow behavior of the material, potentially leading to defects, inconsistencies, or reduced mechanical properties in the final part. Further research and development efforts are necessary to advance the understanding of material behavior, optimize process parameters, and develop intelligent control systems, enabling precise and consistent layer deposition in additive manufacturing processes. By effectively managing layer thickness variations, fabrication sequence optimization can successfully harness the full potential of additive manufacturing technologies, resulting in high-quality, functional, and optimized products. The goal of this research is to find a method to effectively control the thickness of the layers in fabrication sequence optimization. The method should be able to reduce the variation of thickness over the length of the layers and limit the upper and lower bounds of the layer thickness according to user defined values. This will help to bridge the gap between optimized fabrication sequences and the realization of these optimizations.

1.4. Thesis structure

Firstly, the relevant literature is reviewed in chapter 2. In section 2.2 the time component in topology optimization is introduced and in section 2.3 a use case of the fabrication sequence optimization to minimize thermal distortion is discussed. In section 2.5 a method to slice parts into layers of uniform thickness is shown and in section 2.6 a useful method to control layer thickness variation is reviewed. Secondly, in chapter 3 a thickness control method is proposed in a paper. Finally, in chapter 4 shortcomings of the method are discussed, conclusions on this research are drawn and possible future work is suggested.

2

Literature study

2.1. Density based topology optimization

Topology optimization stands as a computational strategy aimed at identifying the most suitable material distribution within a predefined design domain, ensuring specific performance goals are met. One of the most widely used methods in topology optimization is the density-based approach [22]. Instead of directly representing the design's boundary, density-based topology optimization works by assigning a density value to each element of a design domain. These densities can be interpreted as a measure of the presence or absence of material in that particular element.

The core of the topology optimization challenge is the search for an ideal material distribution that minimizes an objective function, operating within applied global volume constraint and supplementary constraints. Here, ρ signifies the material distribution—expressed as a density field—taking either a 0 value (indicative of a void) or 1 (indicating solid) within the design space.

In applying the density-based method, the design domain undergoes a discretization process, transforming into finite elements. This breakdown dictates material distribution by assigning it to N elemental or nodal design variables. However, such discretization can be problematic. When the design variable is restricted to only 0 and 1 values, larger design domains can be especially challenging to optimize. To alleviate this, the continuous density design approach is used, allowing for the implementation of gradient-driven optimization algorithms, improving the convergence.

The mathematical representation of continuous topology optimization can be written as:

$$\underset{\rho\rho}{min} : F(\mathbf{u}(\rho), \rho) = \sum_e \int_{\Omega e} f(\mathbf{u}(\rho_e), \rho_e) dV \tag{2.1}$$

$$s.t. : g_0(\rho) = \int_{\Omega e} \rho(x) dV - V_0 = \sum_e v_e \rho_e - V_0 \leq 0 \tag{2.2}$$

$$: g_i(u(\rho), \rho) \leq 0, i = 1, ..., m \tag{2.3}$$

$$: 0 \leq \rho_e \leq 1 \quad e = 1, ..., N \tag{2.4}$$

$$\tag{2.5}$$

where F is the objective function dependent on the displacement field **u** which is a function of the element densities ρ_e. The optimization is subject to the global volume constraint g_0 with V_0 being the desired maximum volume and additional constraints g_i.

To reduce the complexity of the homogenization approach the SIMP method was introduced to topology optimization. The SIMP (Simplified Isotropic Material with Penalization) method or power-law technique simplifies and improves the convergence of solutions. This relationship between density design variables and material properties gets expressed by a power-law, as shown in Equation 2.6, with E_0 representing the Young's Modulus of solid material, and p being the penalization parameter.

$$E_e(\rho_e) = \rho_e^p E_0 \tag{2.6}$$

For $p = 1$ the optimization problem is a convex problem with a unique solution. However, for the same objective function, when $p > 1$ intermediate densities are penalized in their effective Young's modulus and hence the optimization favors 0-1 solutions. To avoid gray scale elements or too fast convegence, $p = 3$ is the value at which the optimization performs well on both aspects.

When the SIMP method is included, the formulation for compliance minimization will be given by

$$\min_{\rho} : c(\rho) = \mathbf{U}^T \mathbf{K}\, \mathbf{U} = \sum_{e=1}^{N} E_e(\rho_e) \mathbf{u}^T \mathbf{k}_0 \mathbf{u} \tag{2.7}$$

$$s.t. : \mathbf{KU} = \mathbf{F} \tag{2.8}$$

$$: g_0 = \frac{V(\rho)}{V_0} - v_f \leq 0, \tag{2.9}$$

$$: 0 \leq \rho_e \leq 1 \quad e = 1, ..., N \tag{2.10}$$

$$\tag{2.11}$$

where c is the compliance of the structure, evaluated by the displacement field **U** and the global stiffness matrix **K**. The optimization is subject to the global volume constraint where $V(\rho)$ is the material volume of the density field and V_0 is the total volume of the design domain and v_f is the prescribed volume fraction.

2.1.1. MMA solver

The optimization formulation given in Equation 2.7 can be solved using using common optimization algorithms such as Sequential Linear Programming (SLP), Optimality Criteria (OC) and the Method of Moving Asymptotes (MMA). The Method of Moving Asymptotes optimization algorithm [25], characterized by the generation and assessment of strictly convex approximations, is known for its efficiency and robust convergence. This algorithm, using sensitivity calculations [12], derives the objective gradient and constraint function concerning design variables to guide the optimization process.

2.1.2. Sensitivities

The MMA algorithm uses the derivatives of the objective and constraint functions w.r.t. the design variables to guide the optimization in the direction for maximum performance while satisfying the applied constraints. These derivatives are referred to as sensitivities. The sensitivities of the objective function and the global volume constraint in Equation 2.7 are given by

$$\frac{\partial c}{\partial \rho_e} = -p \rho_e^{p-1} E_0 \tag{2.12}$$

$$\frac{\partial g_0}{\partial \rho_e} = \frac{\partial V(\rho)}{\partial \rho_e} \frac{1}{V_0} \tag{2.13}$$

2.1.3. Filtering

To prevent the formation of small feature sizes or checkerboard patterns, a density filtering method is used to smoothen the density field. This density filter is a convolution operator that smoothens the densities ρ_i within a defined filter radius r_d using weighting functions $w(\boldsymbol{x_i}, \boldsymbol{r_d})$. This removes any undesired checkerboard patterns that can occur in density-based optimization. The density filter also offers some form of LSC as it averages the density value of an element with its neighbouring elements. By varying the filter radius, the feature size of the geometries of the design can be changed.

$$\tilde{\rho_e} = \frac{\Sigma_{i \in S_e} w(\boldsymbol{x_i}, r_d) \rho_i}{\Sigma_{i \in S_e} w(\boldsymbol{x_i}, r_d)} \tag{2.14}$$

Here S_e is the set of elements within the prescribed filter radius of a central element. The weight factor $w(\boldsymbol{x_i}, \boldsymbol{r_d})$ is defined by

$$w(\boldsymbol{x_i}, r_d) = max(0, r_d - \Delta(e, i)) \tag{2.15}$$

where $\Delta(e, i))$ is the center-to-center distance of element e to element i. When a density filter is applied to the density field the densitities of the elements become dependent on each other. Therefore, to get accurate sensitivities, a chain rule should be applied when computing the sensitivities with respect to the density variable.

2.2. Space-time topology optimization for additive manufacturing

In the paper *Space-Time Topology Optimization for additive manufacturing* [32], the new topology optimization formulation called *Space-Time Topology Optimization* (STTO) is proposed. Here the structural layout of the design is simultaneously optimized with its fabrication sequence. STTO makes use of two design variables. The structural layout is defined by the density field and the fabrication sequence is defined by the time field $\boldsymbol{t}$. The addition of the time field to the optimization allows the design to be divided in a number of manufacturing stages. On each of these stages, structural performance can be evaluated and constraints can be imposed.

Designs can be optimized for multiple problems, which can be combined in the objective function. For STTO this objective function consists of the performance of the complete design and the performance of the intermediate stages of the design. This leads to a new objective function which is defined by:

$$J(\rho, t) = J_{complete}(\rho, t) + J_{process}(\rho, t) \tag{2.16}$$

In the case of STTO the main objective of the optimization is minimal compliance, which is defined in Equation 2.17. Here **U** is the displacement and **K** is the stiffness matrix. In Equation 2.16 this means that the compliance will be evaluated for each of the intermediate stages and the final design. To impose manufacturability, new objectives can be added to this function or constraints can be added to the optimization.

$$c = \boldsymbol{U^T K(\rho) U} \tag{2.17}$$

The value of the compliance is an indicator of the structural performance of the design. In a later stage, when manufacturability constraints or modifications to the objective function have been applied, this indicator can be used to evaluate the influence on the structural performance. Constraining the optimization is restricting the design freedom and therefore will lead to higher compliances of the design. The effects of the manufacturability constraints can thus be compared to the benchmark value of the unconstrained optimization. The design variables $\boldsymbol{\rho} \in [0, 1]$ and $\boldsymbol{t} \in [0, 1]$ are associated to an element of a discretized design space. The density value should converge to a discrete value of either 0 or 1, where 0 and 1 mean a void or solid element respectively. The time field however is a continuous field ranging from 0 to 1 that indicates the time at which the element is created. The density field consists of a three-field scheme in the optimization. Firstly, a continuous density field is computed from the MMA-solver. The density field is then smoothed by a density filter shown in Equation 2.18. This removes any undesired checkerboard patterns that can occur in density-based optimization. Lastly, the density field is projected using a differentiable threshold projection shown in Equation 2.36. Here β_d controls the sharpness of the step function, and η is the threshold projection value by which the density value of an element is pushed to either 0 or 1.

$$\tilde{\phi_e} = \frac{\Sigma_{i \in S_e} w(\boldsymbol{x_i}, r_t) v_i \tau_i}{\Sigma_{i \in S_e} w(\boldsymbol{x_i}, r_t) v_i} \tag{2.18}$$

$$\rho_e = \bar{\tilde{\phi}}_e = \frac{\tanh(\beta_d \eta) + \tanh\Big(\beta_d(\tilde{\phi_e} - \eta)\Big)}{\tanh(\beta_d \eta) + \tanh(\beta_d(1 - \eta))} \tag{2.19}$$

For the time field, a similar threshold projection is used to cut the total design into a prescribed number of intermediate building stages. To display the density field that is built up until a time threshold T, the time value of the elements lower than that threshold should get to 1 and the time value of the elements built after that threshold should be 0. This is achieved by the formula shown in Equation 2.20.

$$\bar{t}_e^{[T]} = 1 - \frac{\tanh(\beta_t T) + \tanh(\beta_t (t_e - T))}{\tanh(\beta_t T) + \tanh(\beta_t (1 - T))} \tag{2.20}$$

To segmentize the fabrication process, the time field is divided into intervals. With a prescribed number of N intervals, the time at which an intermediate structure (also called stages) is evaluated can be computed by

$$T_i = \frac{i}{N}, \quad i = 0, ..., N \tag{2.21}$$

Using these time points and the threshold projection for the time field shown in Equation 2.20 structural performance of the intermediate structures can be evaluated and constraints can be applied. These constraints can help in making the optimized design more manufacturable. A requirement of the constraints is that they are differentiable. This is necessary to compute the sensitivities that are used in the MMA-solver to optimize the design.

In this paper, it is assumed that the fabrication speed is constant, and thus the maximum volume of the complete structure (V_0) is equally distributed over the time intervals. This means that each of the N stages are bounded by a volume constraint defined by

$$V^{[}T_i] - V^{[}T_{i-1}] \leq \frac{V_0}{N} \quad i = 1, ..., N \tag{2.22}$$

Where $V^{[T_i}$ and $V^{[T_{i-1}}$ are the volume that has been deposited up until the time points T_i and T_{i-1}. In Figure 2.1 a visualisation of the sequence of the intermediate structures is shown.

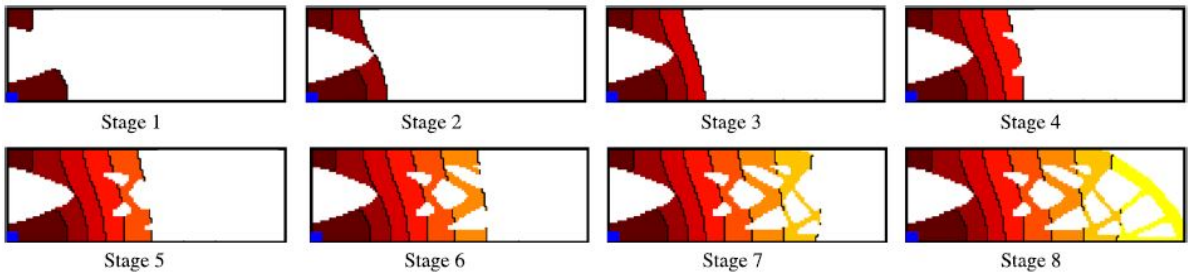

Figure 2.1: Construction sequence of the 8 stages of an optimized structure [32]

To prevent deformation due to self-weight of intermediate structures, supporting structures are often used in additive manufacturing. In the STTO objective formulation shown in Equation 2.23 however, the compliance of the intermediate structures is incorporated to minimize the effect of the self-weight. Here α_i is the weighting factor that defines the contribution of the compliance of the intermediate structures at times T_i to the objective function. This way the part can be produced without additional support structures.

$$\min_{\phi,\tau} c = \boldsymbol{U^T K(\rho) U} + \sum_{i=1}^{N} \alpha_i (\boldsymbol{U}^{[T_i]})^T \boldsymbol{K}(\rho^{[T_i]}) \boldsymbol{U}^{T_i} \tag{2.23}$$

Besides the influence of the self-weight on the compliance, the load of the moving robot platform on top of the structure can also be substantial and can be incorporated into the objective function. Not only does this lead to a minimization of compliance, another important effect of incorporating these process-dependent loads is that they cause the optimization algorithm to create a platform for the robot to move on. The robot should be able to move along the fabricated part of the bridge in order to print the next stage. In Figure 2.2a a visualisation of the moving robot can be seen.

In Figure 2.2b an optimization of a structure including the loads of the weight of the robot at different positions can be seen. The figure shows a varying thickness in the layers. This is due to the fact that the time field is optimized to minimize the compliance due to gravity and process-dependent loads during the fabrication. Another factor of influence for the varying thickness is the varying density field. Even with a smooth time field with isolines equally space apart, the presence (solid) or absence (void) of material within the isolines of the time field can result in variation in the observed layer thickness. The variation in the thickness of the layers should be limited due to manufacturing limitations for the WAAM robot.

(a) Visualisation of the positions and range of the moving robot [32]

(b) Optimized layout and sequence when the loads of the weight of the robot are included

Figure 2.2: Space-time topology optimization using a moving WAAM-robot to account for process dependent loads.

2.3. Fabrication sequence optimization for minimizing distortion in multi-Axis additive manufacturing

In *Fabrication Sequence Optimization for Minimizing Distortion in Multi-Axis Additive Manufacturing* [31] a new objective to optimize the fabrication sequence for is presented. This method optimizes the fabrication sequence of a predefined shape to minimize distortion resulting from thermal strain caused by the manufacturing process such as WAAM fabrication. WAAM generates a lot of heat to melt the material for deposition on the substrate. As the material of the deposited layer solidifies, its volume shrinks as shown in Figure 2.3. The shrinkage of an element is caused by the nodal forces that correspond to the thermal strain.

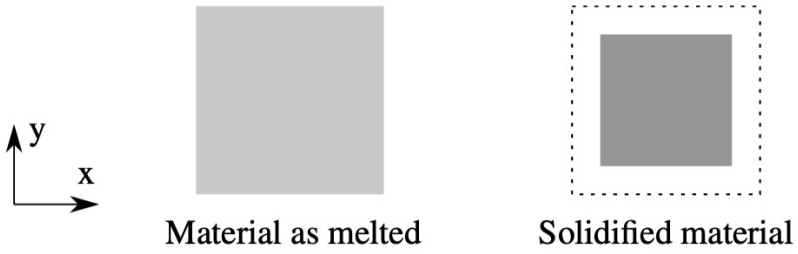

Figure 2.3: Visualisation of the shrinkage of a material element [31]

With the addition of a new layer, the displacements of the $\Delta\mathbf{u}^{[i]}$ resulting from the thermal strains of the elements in the i-th layer, Ω_i, can be computed by solving

$$\mathbf{K}^{[i]}\Delta\mathbf{u}^{[i]} = f^{[i]}, \qquad i = 1, ..., N. \tag{2.24}$$

With this equilibrium equation, we can compute the incremental displacement of the simulation grid due to the addition of each new layer. Under the assumption of small displacements, the displacement field at the i-th stage, $\mathbf{u}^{[i]}$ is computed by the summation of incremental displacements until the current stage,

$$\mathbf{u}^{[i]} = \sum_{i=1}^{i} \Delta\mathbf{u}^{[i]}, \qquad i = 1, ..., N. \tag{2.25}$$

The goal of the proposed method is to minimize these displacements to enhance part quality. In Equation 2.26 the objective function is shown.

$$min \quad d(t) = \mathbf{u}^\top \mathbf{Q}\mathbf{u} \tag{2.26}$$

$$s.t. \quad \mathbf{K}^{[i]}(t)\Delta\mathbf{u}^{[i]} = f^{[i]}(t), i = 1, ..., N, \tag{2.27}$$

$$-\gamma_v \leq g_i(t) \leq 0, i = 1, 2, ..., N, \tag{2.28}$$

$$g_0(t) \leq \gamma_c \tag{2.29}$$

$$0 \leq t_e \leq 1, \forall e \tag{2.30}$$

Here, **u** contains the displacements of the nodes of the elements and **Q** is a sparse matrix to specify the nodal displacements of concern. The displacement of a node is computed by

$$d_i = (u_i^x)^2 + (u_i^y)^2 \tag{2.31}$$

The optimization problem is solved by using a gradient-based optimization (MMA), with the only design variable being the time values t placed on the nodes of the elements. The element time value is then computed by taking the average of the nodes. From these elemental time values the fabrication sequence can be determined. In Figure 2.4 the distortion resulting from fabrication using regular planar layers can be compared to the sequence optimized to minimize distortion.

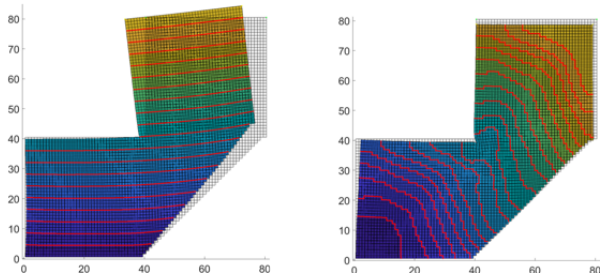

Figure 2.4: Fabrication sequence optimization for distortion resulting in varying layer thickness [31]

While the method is succesful in reducing the distortion of the fabricated part, the resulting layers show large variation in thickness. For manufacturability reasons, the thickness of the layers should be as constant as possible as fabrication methods like WAAM have a limited flexibility in varying the thickness of the deposited layer. The variation in layer thickness is a problem occurring in STTO as well, and needs to be solved by controlling the optimization to limit thickness variation. The optimization for distortion favours a certain fabrication sequence resulting in the varying layer thickness. Modifying the optimization objective and constraints can improve manufacturability at cost of the distortion of the part.

2.4. Robust formulation

There are many proposed methods in topology optimization for imposing length scale control on the design [8] [7] [37]. Typically, these length scale control methods work on the entire design. One of the most used methods is the so called robust formulations [30]. This method makes use of an optimization formulation based on erosion, intermediate and dilation projections. These projections create three designs that are tested on their compliance using a FEM-calculation. These compliances are then used in the objective function which is shown in Equation 2.32.

$$\begin{aligned} &\min_{\rho} : max(\boldsymbol{f}(\bar{\tilde{\rho}}^e(\rho)), \boldsymbol{f}(\bar{\tilde{\rho}}^i(\rho)), \boldsymbol{f}(\bar{\tilde{\rho}}^d(\rho)) \\ &s.t. : \boldsymbol{K}(\bar{\tilde{\rho}}^e)\boldsymbol{u}^e = \boldsymbol{f} \\ &s.t. : \boldsymbol{K}(\bar{\tilde{\rho}}^i)\boldsymbol{u}^i = \boldsymbol{f} \\ &s.t. : \boldsymbol{K}(\bar{\tilde{\rho}}^d)\boldsymbol{u}^d = \boldsymbol{f} \end{aligned} \tag{2.32}$$

Where the superscripts e, i and d stand for the eroded, intermediate and dilated designs respectively. In the case of compliance optimization, the eroded case will always have the highest compliance due to its more slender geometry. Therefore, the problem formulation can often be reduced to the formulation shown in Equation 2.34. In the case of STTO however, the objective function consists of the compliance of the final structure and the compliances of the intermediate structures due to density-dependent loads (self-weight). The compliance due to self-weight can have a non-monotonous character [2]. As this compliance is part of the objective function shown in Equation 2.23, the objective function itself can become non-monotonous as well. This is dependent on factors such as the weight-factor α, the number of stages N for which the compliance is computed and the load on the finalized structure F.

Besides the non-monotonous character of the compliance due to self-weight, the paper points out another undesirable effect of density-dependent loads in the optimization. The compliances of the intermediate structures are dependent on the ratio of the gravity g and the stiffness K. Using the Solid Isotropic Material with Penalization (SIMP) method, the elasticity modulus for an element is determined as shown in Equation 2.33.

$$E_i = \rho_i^p E_0 \tag{2.33}$$

Here $\rho \in [0, 1]$ is the density parameter, p is the penalization factor which is often set to 3, and E_0 is the elasticity modulus of the material. Because the stiffness is related to the E-modulus the ratio $g\ \rho\boldsymbol{\nabla} \cdot K\ \rho^p$ becomes related to the density parameter. This can cause problems when the pseudo-density tends to zero, which means that the ratio and thus the compliance goes to infinity. The algorithm tries to solve this problem by increasing the density slightly to reduce the nodal displacements. Similar problems can occur when using the threshold projection for the robust formulation. The projections can push the elemental densities to low, non-zero values which affect the ratio thus the compliance. It is therefore proposed in the paper to use a modified version of the SIMP-method, which reduces this effect. Although reduction of the formulation has the advantage of reducing computational effort of the optimization, one can not simply assume the possibility of the reduction. The effects of the density-dependent loads on the objective function should first be analysed before a reduced formulation can be used.

On the three projections of the original (non-reduced) robust formulation, constraints are imposed. The volume constraints on the optimization are imposed using the volumes of the dilated designs. This is because the dilated design has the highest volume, and thus violation of the desired volume fraction will make the MMA-solver direct the volume of the density-field down to comply with the constraint. The volume constraint is shown in Equation 2.35. Here the summation of the density of the elements is taken and divided by the total volume of the design space. The volume fraction V_d^* of the dilated structure is updated every 20 iterations such that the volume of the intermediate design V_i becomes equal to V^*. The intermediate structure will then eventually be used as the blueprint design.

$$\begin{aligned} &\min_{\rho} : \boldsymbol{f}(\bar{\tilde{\rho}}^e(\rho)) \\ &s.t. : \boldsymbol{K}(\bar{\tilde{\rho}}^e)\boldsymbol{u}^e = \boldsymbol{f} \end{aligned} \tag{2.34}$$

$$f_v(\rho) = \frac{\Sigma_i \bar{\tilde{\rho}}_i^d v_i}{V} \leq V_d^* \tag{2.35}$$

Reducing the formulation helps lowering the computational cost of the optimization. As the eroded structure always has the highest compliance, the FEM-calculations of the intermediate and dilated designs can be left out. As FEM-calculations are computationally costly, this has a positive effect on the duration of each loop of the optimization. It should be noted however, that when optimization is extended to other problems such as heat conduction, the eroded topology might not always be the worst performing. In this case, the robust formulations cannot be reduced to the formulation shown in Equation 2.34 and thus the complete formulation shown in Equation 2.32 should be used.

The robust formulation method generates the eroded, intermediate and dilated designs by making use of the threshold projection shown in Equation 2.36. For each of the cases, the threshold parameter η is different, with the dilated structure having the lowest threshold ([0,1]), the intermediate structure in the middle ($\eta = 0.5$) and the eroded structure having the highest threshold projection value. This leads to the following threshold projections:

$$\begin{aligned}
\rho_e = \bar{\tilde{\phi}}_e &= \frac{\tanh(\beta_d \eta_e) + \tanh\Big(\beta_d(\tilde{\phi}_e - \eta_e)\Big)}{\tanh(\beta_d \eta_e) + \tanh(\beta_d(1 - \eta_e))} \\
\rho_i = \bar{\tilde{\phi}}_e &= \frac{\tanh(\beta_d \eta_i) + \tanh\Big(\beta_d(\tilde{\phi}_e - \eta_i)\Big)}{\tanh(\beta_d \eta_i) + \tanh(\beta_d(1 - \eta_i))} \\
\rho_d = \bar{\tilde{\phi}}_e &= \frac{\tanh(\beta_d \eta_d) + \tanh\Big(\beta_d(\tilde{\phi}_e - \eta_d)\Big)}{\tanh(\beta_d \eta_d) + \tanh(\beta_d(1 - \eta_d))}
\end{aligned} \tag{2.36}$$

The projection parameter β_d controls the sharpness of the threshold projection function. This parameter is increased during the optimization to create a near discrete density-field of void (0) and solid (1) elements. In the paper, the beta parameter is doubled every 50 iterations. The optimization is sensitive to the projection parameters β, and its increasement, and η. Slower increasement of beta allows for better convergence but increases the amount of iterations required for the optimization to converge, so this results in a trade-off. As shown in Figure 2.5b, when increasing these parameters correctly, the optimization converges to a black and white design. When comparing Figure 2.5a to Figure 2.5b, it can be seen that the robust formulations do indeed impose length scale control on the final design.

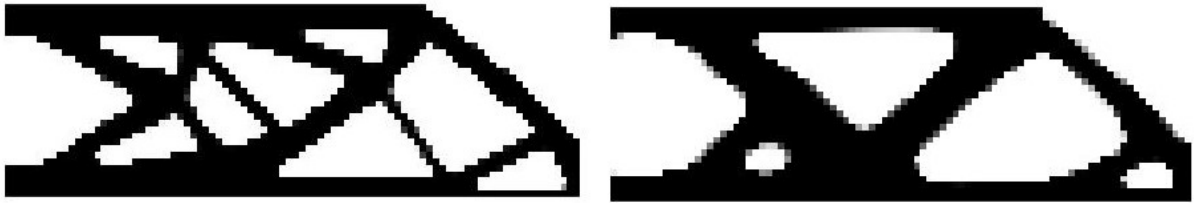

(a) Optimization without robust formulations **(b)** Optimization using tuned parameters

Figure 2.5: Effect of the robust formulations on the design

Although the robust formulations do impose LSC on both the void and solid phase, they are typically used for the final design. In STTO however, robustness and thus manufacturability is also required on the intermediate structures. The robust formulations do not ensure that LSC is imposed on each individual layer. This means the formulations are useful to minimize feature size in the design, but can not control the variation in thickness of the layers.

2.5. Slicing methods for uniform thickness

To produce parts generated by Topology Optimization or CAD-models using additive manufacturing, the part needs to be divided into printable layers. For this, so called slicing software is used to determine the path in the plane of each layer. Conventional slicing algorithms for additive manufacturing slice the part into planar layers of fixed thickness [9]. The simplicity and robustness of this slicing method makes it suitable for most designs and AM equipment. However, the introduction of multi-axis additive manufacturing offers possibilities to improve surface finishing, create support-free structures and optimize the fabrication sequence for process dependent physics problems [35]. To utilize the capabilities of multi-axis AM, slicing algorithms able to divide the designed part into curved layers are needed. To be able to slice the part in curved layers a heat method can be used [19] [4]. In this method, the part is virtually placed on a heated base plate of temperature T_{bottom} with the top surface has a fixed temperature of T_{top}. The temperature differences of the bottom and top boundaries will cause the heat to spread out through the part as time goes by as shown in Figure 2.6. The heat equation shown in Equation 2.37 is used to solve this heat transfer problem.

$$\frac{\rho C_p \partial T}{\partial t} = k\Delta T \tag{2.37}$$

With the temperature field obtained from the solved heat equation the isothermal surfaces can now be extracted from the geometry. As the temperature does not decrease linearly over the height of the part, the distance between isothermal surfaces for a fixed temperature gap will also decrease nonlinearly. Therefore the average magnitude of the temperature gradient over a layer is used to determine the next isothermal surface, as shown in Equation 2.38.

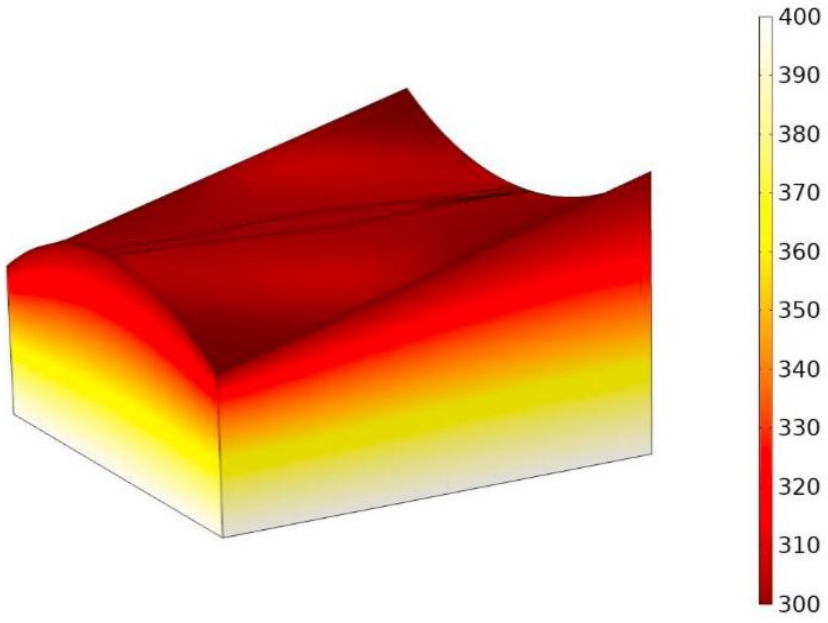

Figure 2.6: Simulated temperature field for isothermal slicing [19]

$$T_i = T_{i-1} - d \cdot |\bar{\Delta T}| \tag{2.38}$$

Here T_i is the temperature of the next isothermal surface, T_{i-1} is the temperature of the current isothermal surface, d is the desired thickness of the layer and $|\bar{\Delta T}|$ is the average magnitude of temperature gradient over this layer. Similarly, a time field can be used instead of a temperature field to determine the isosurfaces. For the time field however, the magnitude of the gradient over a layer of thickness d will be added to the previous value of the isoline as shown in Equation 2.39

$$T_i = T_{i-1} + d \cdot |\bar{\Delta T}| \tag{2.39}$$

2.6. Layer thickness control

In recent work a method to control the variation of the layer thickness has been proposed for multi-axis AM. [6]. Firstly a method to generate curved layers for multi-axis 3D printing is used by following an optimized scalar field $G(\boldsymbol{x})$. From this field surface layers can be generated by extracting iso-lines of $G(\boldsymbol{x})$. The distance between these iso-lines is the thickness of the layer, which can vary along the boundary. As the WAAM manufacturing hardware has limits in varying the thickness of the deposited layer, this should be controlled when optimizing. To achieve this, the formula shown in Equation 2.40 can be added to the objective function.

$$E_t = \sum V_e(\|\nabla G(\boldsymbol{x_e})\| - c)^2 \tag{2.40}$$

Here the magnitude of the gradient of $G(\boldsymbol{x})$ indicates the speed of the material deposition, c is the target layer thickness of each layer and V_e is the volume of an element. When the magnitude of the gradient of $G(\boldsymbol{x})$ is optimized to be nearly constant, it is possible to control the variation of the thickness to make it as uniform as possible. Such a formulation can be incorporated in the objective function of fabrication sequence optimization to control the layer thickness variation, which will improve the manufacturability. The addition of this formulation to the objective function can also have a positive effect on the thickness computation mentioned in section 2.5. As the gradients within a layer will vary less, the computed thickness from the gradient magnitudes within that layer will be more accurate.

2.7. Gap in the state of the art

While slicing algorithms do exist as post optimization process to slice parts in layers of uniform thickness, such methods have not been incorporated in the optimization yet. With the introduction of a time component to the (topology) optimization process, the toolpath can now be incorporated in the optimization. As the fabrication sequence can be optimized for objectives such as minimizing distortion, the optimized sequence can result in varying layer thickness. While there are several length scale control methods for minimizing and maximizing feature sizes in the design domain, no method has been developed yet to do this layer-by-layer to generate a optimized sequence feasible for additive manufacturing. Hence to make such optimized sequences feasible for production, a method needs to be developed to control the thickness of all the layers such that they are manufacturable for the multi-axis AM-equipment.

3

Layer thickness control in fabrication sequence optimization for additive manufacturing

Abstract

With the introduction of a time component for topology optimization in recent work, fabrication-process-dependent physics can now be incorporated in the optimization process. The fabrication sequence resulting from such complex optimizations can lead to layers with large variations in thickness. For manufacturability reasons, this variation should be controlled. In this paper, we present a method to control the variation in thickness of the projected layers to improve the manufacturability. We use the continuous pseudo-time field and its gradients to track the development of the layer boundaries. To demonstrate the effectiveness of the method, we apply the control method on a fabrication sequence optimization for minimizing distortion. The results show that the control method is able to reduce the variation of thicknesses compared to the original sequence optimization for minimizing distortion.
[1]

[1] This chapter was intended as a part of a manuscript for a journal submission.

3.1. Introduction

The use of multi-axis robotic systems in additive manufacturing has increased the manufacturing flexibility. Instead of the standard planar layer deposition, with a printing nozzle or building plate that can rotate during the fabrication, additive manufacturing along a curved surface is now a possibility[26] [5] [6]. In conventional additive manufacturing, the fabrication sequence is uniquely determined when a building orientation of the component is given, due to the planar stacking of the layers. With the introduction of multi-axis additive manufacturing however, the number of possible fabrication sequences is increased. Due to this improvement in additive manufacturing, finding the optimal fabrication sequence to improve the quality of the fabricated part poses a new challenge.

Currently, the slicing of parts into printable layers is mostly considered a geometric problem, which is typically done post optimization. While literature shows several methods to slice these parts into curved layers and account for manufacturability [19] [24] [1], the physical effects of the resulting printing sequence are not considered [18]. In a recent study a new type of optimization, called Space-Time Topology Optimization (STTO) [32] was proposed. In this method the optimization is done concurrently on both the structural layout of the design and the fabrication sequence [29]. The fabrication sequence can be derived from the psuedo-time field. In following work [31] the possibility of fabrication sequence optimization for minimizing distortion using such a pseudo-time field was demonstrated. The addition of the time-field in the optimization process offers opportunities to optimize for complex fabrication-process-dependent physics problems [18] [16] [15]. The performance of the part can then be simulated layer-by-layer [13].

A limiting factor in optimizing the fabrication sequence of such problems is the manufacturability. In the optimization for minimizing distortion [31] it can be seen that the optimized fabrication sequence leads to non-uniform layer thickness. While some additive manufacturing methods, such as Wire-Arc Additive Manufacturing (WAAM) [33] can control the thickness of the deposition, the flexibility is limited [21] [10] [11]. Depending on the WAAM equipment specifications, the thickness of a layer has a lower and an upper bound, and thus allows a limited variation in thickness of a layer. To be able to combine the slicing of the part into the optimization process, manufacturability has to be taken into account. Therefore, to make such optimized sequences feasible for fabrication, these restrictions should be incorporated in the optimization process.

The aim for this paper is to propose a method to control the variation in thickness of the layers to ensure manufacturability of fabrication sequence optimized designs. The optimization for minimizing distortion is chosen to validate the effectiveness of the method, but the proposed methods should not be limited to this specific type of optimization. The structure of the paper is as follows. In section 3.2 background information is given and the problem is identified. In section 3.3 the proposed method is explained. In section 3.4 we present the results from the proposed method to control the layer thickness during the optimization process after which conclusions are drawn and future work is suggested.

3.2. Layer thickness variation in sequence optimization

In Figure 3.1a and Figure 3.1b we can see the optimized time fields to minimize distortion of a part for two different intitial time fields. The figures clearly show the variation in layer thickness of the optimized sequences. While the optimization is successful in reducing the distortion of the part, the resulting projected layers are not feasible for manufacturing due to the large thickness variations. The variation in thickness of the optimized layers are also influenced by the shape of the part, its mesh size and number of layers, and the initialized time field. However, the optimization should not solely be dependent of initialization parameters and thus further control on the thickness of the layers is required.

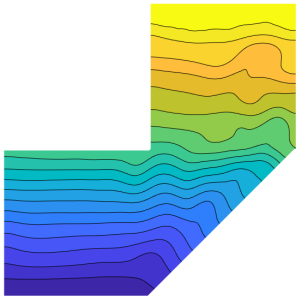

(a) Original optimization for minimizing distortion
Obj: distortion = 2.0E-4

(b) Original optimization for minimizing distortion
Obj: distortion = 1.7E-4

Figure 3.1: Optimized fabrication sequences to minimize distortion for two different initial time fields

3.3. Layer thickness control

In this section we propose a framework to control the variation in layer thickness in fabrication sequence optimization. Firstly the objective function, based on gradient control, is explained. The formulation of the optimization problem is then given in subsection 3.3.1 followed by a sensitivity analysis in subsection 3.3.5.

3.3.1. Variation of layer thickness

In fabrication sequence optimization the time values of the elements are derived from the time values on its nodes by taking the average of the four nodes, as shown in Figure 3.2. These time values represent the order in which the elements of a part are fabricated. The time field is a psuedo-time field where $t \in [0, 1]$. Elements can have equal or similar time values to form isolines in the time field. The gradients in x and y-direction of an element can be determined from the nodal time values as shown in Equation 3.1.

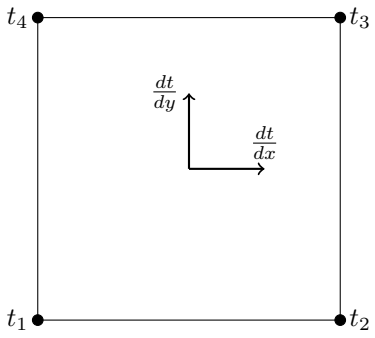

Figure 3.2: Element with its corresponding nodes

$$t_e = \frac{t_1 + t_2 + t_3 + t_4}{4} \tag{3.1}$$

$$\frac{dt}{dx} = \frac{1}{2}(t_2 - t_1) + \frac{1}{2}(t_3 - t_4) \tag{3.2}$$

$$\frac{dt}{dy} = \frac{1}{2}(t_4 - t_1) + \frac{1}{2}(t_3 - t_2) \tag{3.3}$$

The magnitude of the gradient of an element in the 2D time field is then computed using Equation 3.4. By taking the magnitude of the gradients w.r.t. the x- and y-position, the development of the isolines in the normal direction can be tracked. This is the direction of interest to control the distance between specified isolines in the time field.

$$M = \|\nabla T\| = \sqrt{\left(\frac{dt}{dx}\right)^2 + \left(\frac{dt}{dy}\right)^2} \tag{3.4}$$

To control the thickness of the layer along its length, the gradients within that layer have to be controlled. Similar magnitudes of the gradients over the length of the layer will result in similar thickness. Some variation is allowed but for manufacturability reasons the layers should be as uniform as possible. To control the uniformity of the layers, a formulation shown in Equation 3.5 is added to the objective function. This objective function resembles the variance function commonly used for statistics. By reducing the variance of the gradient magnitudes within the layers the variation in layer thickness can be controlled.

$$obj : min : G(t, T_p) = \sum_{i=1}^{i=N} \left(\bar{t}_e^{[T_p(i+1)]} - \bar{t}_e^{[T_p(i)]}\right) \left(M^j - m_t^i\right)^2 \tag{3.5}$$

Here M^i denotes the gradient magnitudes of the elements within the layer and m_t^i is the magnitude target defined as the average of the magnitudes within each layer, as shown in Equation 3.6. The value of the magnitude targets are bound by the upper and lower limit of the time field.

$$m_t^i = \frac{\sum_e M \cdot \left(\bar{t}_e^{[T_p(i+1)]} - \bar{t}_e^{[T_p(i)]}\right)}{\sum_e \rho_e \cdot \left(\bar{t}_e^{[T_p(i+1)]} - \bar{t}_e^{[T_p(i)]}\right)} \tag{3.6}$$

$$\bar{t}_e^{[T]} = 1 - \frac{\tanh(\beta_t T_p) + \tanh(\beta_t (t_e - T_p))}{\tanh(\beta_t T_p) + \tanh(\beta_t (1 - T_p))} \tag{3.7}$$

The threshold projections $\bar{t}_e^{[T_p]}$ are used here to isolate the gradient magnitudes within each of the layers from entire magnitude field. This way we can evaluate the average gradient magnitude within a layer. The slope of the projections are determined by the sharpness parameter β. To evaluate the average magnitude within each layer more accurately, the sharpness parameter can be increased. This creates a sharper cut-off at the time points T_p as shown in Figure 3.3a and Figure 3.3b. By more accurately evaluating the average gradient magnitude within the layers, the variance of these gradient magnitudes can be controlled better.

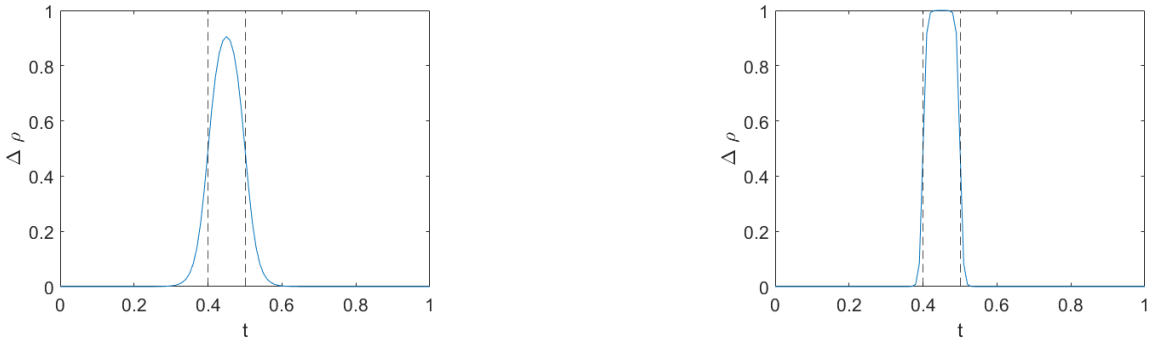

(a) Isolated layer for $\beta = 30$

(b) Isolated layer for $\beta = 100$

Figure 3.3: Isolation of the layers using threshold projection on the time field

3.3.2. Manufacturability constraints on layers

To ensure the optimized fabrication sequence is feasible for production, we impose constraints to improve the manufacturability. Firstly we impose a fabrication speed constraint. For simplicity, we assume a constant fabrication speed. Previously this was enforced by constraining the volume at predefined time points, as shown in Equation 3.8 where these time points T_p represent the values of the isolines which will form the upper and lower boundary of a layer. For a constant and uniform thickness however, a fixed layer volume limits the length of the layer and thus the design freedom as the desired thickness

of the layer is defined should remain constant. The volume constraint is therefore modified by making the time points a design variable. This makes varying the length and thus volume of the layers possible while ensuring a constant fabrication speed. Since the number of layers is prescribed as *N*, the volume up until the i-th layer shall be $T_p(i) \cdot V^*$,

$$V^{[i]}(t) = \sum_e \rho_e^{[i]}(t_e) \cdot v_e = \frac{i}{N} V^*, i = 1, ..., N, \tag{3.8}$$

$$V^{[i]}(t) = \sum_e \rho_e^{[i]}(t_e) \cdot v_e = T_p(i) \cdot V^*, \qquad i = 1, ..., N, \tag{3.9}$$

where v_e is the volume of an element and $T_p(i)$ is the time point at which the i-th layer is deposited. The above equality constraint is replaced by two inequality constraints for the upper and lower bound for the fabrication speed respectively, as shown in Equation 3.10. The constraint can be relaxed accordingly to allow variation in fabrication speed.

$$g_1^i(t, T_p) = V^{[i]}(t) - T_p(i) \cdot V^* \leq 0, \qquad i = 1, ..., N, \tag{3.10}$$

$$g_2^i(t, T_p) = T_p(i) \cdot V^* - V^{[i]}(t) \leq 0, \qquad i = 1, ..., N, \tag{3.11}$$

Secondly we impose a thickness constraint on each of the *N* layers to control the upper and lower limit of the thickness. In Equation 3.12 the formula used to evaluate the thickness of each layer is used.

$$d_i = \frac{\Delta t}{\overline{M}} = (T_p(i+1) - T_p(i)) \cdot \frac{\sum_e \rho_e \cdot \left(\bar{t}_e^{[T_p(i+1)]} - \bar{t}_e^{[T_p(i)]} \right)}{\sum_e M \cdot \left(\bar{t}_e^{[T_p(i+1)]} - \bar{t}_e^{[T_p(i)]} \right)} \approx d_{target} \tag{3.12}$$

Where d_{target} is the target thickness of the layer. This target thickness can be determined depending on fabrication equipment parameters, but in this work we determine it based on the part dimension h and the number of stages N as shown in Equation 3.15. The above equality constraint is replaced by two inequality constraints for the upper and lower bound respectively, as shown in Equation 3.13.

$$g_3^i(t, T_p) = d_i - d_{max} \leq 0, \qquad i = 1, ..., N, \tag{3.13}$$

$$g_3^i(t, T_p) = d_{min} - d_i \leq 0, \qquad i = 1, ..., N, \tag{3.14}$$

$$d_{target} = \frac{h}{N} \tag{3.15}$$

The thickness constraint can be relaxed to allow deviation from the target thickness by using upper and lower bounds d_{max} and d_{min}.

As the time points T_p are now a design variable and the volumes of the layers are no longer bound. To prevent the time points from overlapping or layers becoming too small, a minimum volume constraint is added to control the minimum dimensions of the deposited layers. The minimum volume inequality constraint is shown in Equation 3.16,

$$g_4^i = V_{min} - \sum \rho \cdot (ft(t) - gt(t)) \leq 0, \qquad i = 1, ..., N, \tag{3.16}$$

where V_{min} denotes the minimum required each layer. With the thickness of the layers controlled by the thickness constraint, this ensures that each layer satisfies a minimum length. In the case of WAAM this would correspond to the minimum dimensions of the weld bead.

3.3.3. Continuity constraint

As the proposed thickness control formulation controls the magnitude of the gradients within a layer but not the direction, local minima and maxima can occur in the time field. These local minima and maxima correspond to isolated material patches and enclosed voids, respectively. As enclosed voids are inaccessible and isolated material patches require support structures, these are undesired for manufacturability reasons. To prevent these from occurring, we use a continuity constraint [31] shown in Equation 3.17

$$g_0(t) = \frac{1}{n\left(\mathcal{M}\right)} \sum_{e \in \mathcal{M}} \| t_e - mean_{i \in \mathcal{N}_1}(t_i) \|^2 \leq \gamma_c, \tag{3.17}$$

where $\mathcal{M}$ is the set of all elements in the domain except for the starting region for the fabrication process and $\mathcal{N}_1$ is the set of elements adjacent to element e. The γ_e parameter is a small constant used for numerical stability. The mean value of these adjacent elements is evaluated as shown in Equation 3.18.

$$mean_{i \in \mathcal{N}_1}(t_i) = \frac{\sum_{i \in \mathcal{N}_1} t_i}{n\left(\mathcal{N}_1\right)} \tag{3.18}$$

3.3.4. Optimization problem formulation

The original aim of the optimization was to reduce the distortion of the fabrication component. To improve manufacturability, a term is added to the objective function for the uniform thickness of the layers and constraints are added. The modified optimization problem is formulated as

$$\begin{aligned}
min \quad & G(t, T_p) = \mathbf{u}^\top \mathbf{Q} \mathbf{u} + \sum_{i=1}^{i=N} \alpha_u \left(\bar{t}_e^{[T_p(i+1)]} - \bar{t}_e^{[T_p(i)]} \right) (M^i - m_t^i)^2 && (3.19)\\
s.t. \quad & \mathbf{K}^{[i]}(t) \Delta \mathbf{u}^{[i]} = f^{[i]}(t), \qquad i = 1, 2, ..., N, && (3.20)\\
& g_0(t) \leq \gamma_c && (3.21)\\
& g_1(t, T_p) \leq 0 && (3.22)\\
& g_2(t, T_p) \leq 0 && (3.23)\\
& g_3(t, T_p) \leq 0 && (3.24)\\
& g_4(t, T_p) \leq 0 && (3.25)\\
& 0 \leq t_e \leq 1, \forall e && (3.26)\\
& 0 \leq T_p(i) \leq 1, \qquad i = 1, 2, ..., N, && (3.27)
\end{aligned}$$

where α_u is the weighting factor of the uniform thickness objective. This weighting factor can be adjusted to allow more or less variation in layer thickness. The optimization problem is solved by gradient-based numerical optimization using the Method of Moving Asymptotes (MMA) [25].

3.3.5. Sensitivity analysis

The sensitivities of the distortion objective with respect to the time t are known from previous work [31] and will not be shown here. The sensitivity of the layer thickness control part of the objective function with respect to the design variables t_e and T_p are given by

$$\begin{aligned}
\frac{\partial G}{\partial t_e} = & \sum_{i=1}^{i=N} \alpha_u \left(\frac{\partial \bar{t}_e^{[T_p(i+1)]}}{\partial t_e} - \frac{\partial \bar{t}_e^{[T_p(i)]}}{\partial t_e} \right) \left(M - m_t^i \right)^2 \\
& + \sum_{i=1}^{i=N} 2 \cdot \alpha_u \left(\bar{t}_e^{[T_p(i+1)]} - \bar{t}_e^{[T_p(i+1)]} \right) \left(M - m_t^i \right) \frac{\partial M}{\partial t_e} \\
& + \sum_{i=1}^{i=N} -2 \cdot \alpha_u \left(\bar{t}_e^{[T_p(i+1)]} - \bar{t}_e^{[T_p(i)]} \right) \left(M - m_t^i \right) \frac{\partial m_t^i}{\partial t_e}
\end{aligned} \tag{3.28}$$

$$\frac{\partial G}{\partial T_p} = \sum_{i=1}^{i=N} \alpha_u \left(\frac{\partial \bar{t}_e^{[T_p(i+1)]}}{\partial T_p} - \frac{\partial \bar{t}_e^{[T_p(i)]}}{\partial T_p} \right) \left(M - m_t^i\right)^2 + \sum_{i=1}^{i=N} 2 \cdot \alpha_u \left(\bar{t}_e^{[T_p(i+1)]} - \bar{t}_e^{[T_p(i)]} \right) \left(M - m_t^i\right) \frac{\partial M}{\partial T_p} + \sum_{i=1}^{i=N} -2 \cdot \alpha_u \left(\bar{t}_e^{[T_p(i+1)]} - \bar{t}_e^{[T_p(i)]} \right) \left(M - m_t^i\right) \frac{\partial m_t^i}{\partial T_p} \tag{3.29}$$

Where $\frac{\partial \bar{t}_e^{[T_p]}}{\partial t_e}$, $\frac{\partial M}{\partial t_e}$, $\frac{\partial m_t^i}{\partial t_e}$, $\frac{\partial \bar{t}_e^{[T_p]}}{\partial T_p}$, $\frac{\partial M}{\partial T_p}$ and $\frac{\partial m_t^i}{\partial T_p}$ can be evaluated from Equation 3.7, Equation 3.4 and Equation 3.6.
With the time points T_p now being design variables, the objective to minimize distortion is now also dependent on these design variables. Therefore we need to evaluate the sensitivities of the distortion objective w.r.t. these variables. In Equation 3.30 the objective function for minimizing distortion is given.

$$L(t, T_p) = \mathbf{u}^T \mathbf{Q}\, \mathbf{u} + \sum_{i=1}^{i=N} \lambda_t^T \left(\mathbf{K}^{[i]}(t, T_p) \Delta u^{[i]} - f^{[i]}(t, T_p) \right) \tag{3.30}$$

The resulting finite difference sensitivity check of the objective function and constraints with respect to the design variables can be seen in Appendix B.

$$\frac{\partial L(t, T_p)}{\partial T_p} = \sum_{i=1}^{i=N} \left(2\mathbf{u}^T \mathbf{Q} + \lambda_i^T \mathbf{K}^{[i]}(t, T_p) \right) \frac{\partial \Delta u^{[i]}(t, T_p)}{\partial T_p} + \sum_{i=1}^{i=N} \lambda_t^T \left(\frac{\partial \mathbf{K}^{[i]}(t, T_p)}{\partial T_p} \Delta u^{[i]}(t, T_p) - \frac{\partial f^{[i]}(t, T_p)}{\partial T_p} \right) \tag{3.31}$$

We choose λ_i satisfying

$$\mathbf{K}^{[i]}(t, T_p)\lambda_i + 2\mathbf{Q}^T \mathbf{u} = 0, \qquad i = 1, 2, ..., N. \tag{3.32}$$

This simplifies Equation 3.31 to

$$\frac{\partial L(t, T_p)}{\partial T_p} = \sum_{i=1}^{i=N} \lambda_t^T \left(\frac{\partial \mathbf{K}^{[i]}(t, T_p)}{\partial T_p} \Delta u^{[i]}(t, T_p) - \frac{\partial f^{[i]}(t, T_p)}{\partial T_p} \right) \tag{3.33}$$

The stiffness matrix **K** depends on density of the elements. These densities are a function of the time value of the element and the time points T_p at which the layers are deposited and the constraints are evaluated. Using the chain rule, the resulting derivative of the stiffness matrix w.r.t the time points is

$$\frac{\partial \mathbf{K}_e^{[i]}(t, T_p)}{\partial T_p} = \frac{\partial \mathbf{K}_e^{[i]}(\rho_e^{[i]})}{\partial \rho_e^{[i]}} \frac{\partial \rho_e^{[i]}}{\partial \bar{t}_e^{[i]}} \frac{\partial \bar{t}_e^{[i]}}{\partial T_p} \tag{3.34}$$

3.4. Results

The proposed method has been implemented using Matlab. In this section, we will present the results of the optimization of the fabrication sequence to control layer thickness in Wire Arc Additive Manufacturing (WAAM) on 2D components. The goal of the optimization is to ensure that the layers are uniform in thickness, especially for WAAM where highly varying layer thicknesses are difficult to manufacture. A parameter study was done to show the influence of the weight factor of the uniform thickness objective. The optimization was performed using the computational framework for fabrication sequence optimization presented in the paper *Fabrication sequence optimization for minimizing distortion in multi-axis additive manufacturing*. The fabrication sequence was encoded by a continuous pseudo-time field and optimized using gradient-based numerical optimization. The objective of the optimization was to minimize distortion in multi-axis additive manufacturing while controlling the variation in thickness of the layers. The distortion is evaluated by the displacements of the specified nodes by

$$d_i = (u_i^x)^2 + (u_i^y)^2 \tag{3.35}$$

where subscript i refers to the index of the node of interest and the superscripts x and y indicate the x and y parts of the displacement vector.

3.4.1. L-shape

We first test the method on a 2D L-shaped component shown in Figure 3.4a. The domain is discretized by a finite element grid of 180 x 120 with 20 layers. The bottom of the part is fixed to the horizontal build plate. We use two different fabrication starts as reference to initialize the time field t, from the bottom left and from the entire build plate on the bottom. A distance field corresponding to the left bottom starting point is shown in Figure 3.4c.

(a) Given L-shape component **(b)** Nodes of interest **(c)** Initial time field from the bottom

Figure 3.4: Initialization of the design domain

For comparison the original optimizations for minimizing distortion for the L-shape are given in Figure 3.5a and Figure 3.5b. The optimizations were done using the same parameter settings, with two different initial time fields. It shows that in the original optimizations to minimize the distortion for the L-shape component, the optimized fabrication sequence resulted in large variation in thickness of the layers.

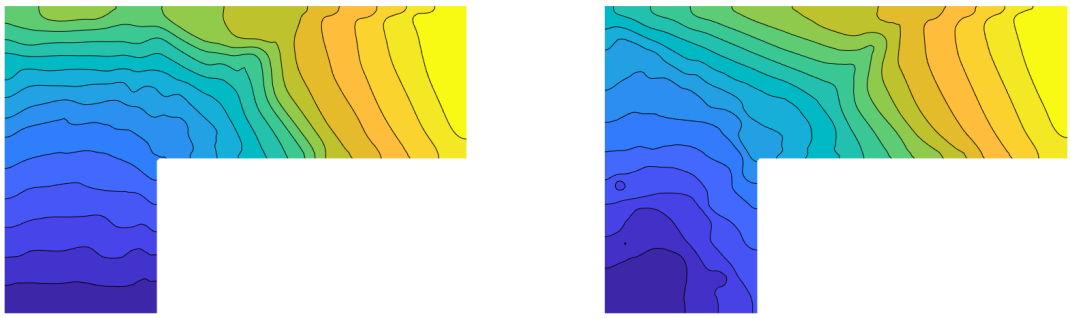

(a) Obj: distortion = 1.0e-4 **(b)** Obj: distortion = 2.0E-4

Figure 3.5: Optimized fabrication sequences to minimize distortion without layer thickness control for two different initial time fields

In Figure 3.6a and Figure 3.6b the fabrication sequences are shown using the proposed layer thickness control method. Both results show an improvement in reducing the layer thickness variation when compared to the original optimizations. The added design variables T_p allow the layers vary their length while effectively maintaining a constant thickness as imposed by the thickness constraint.

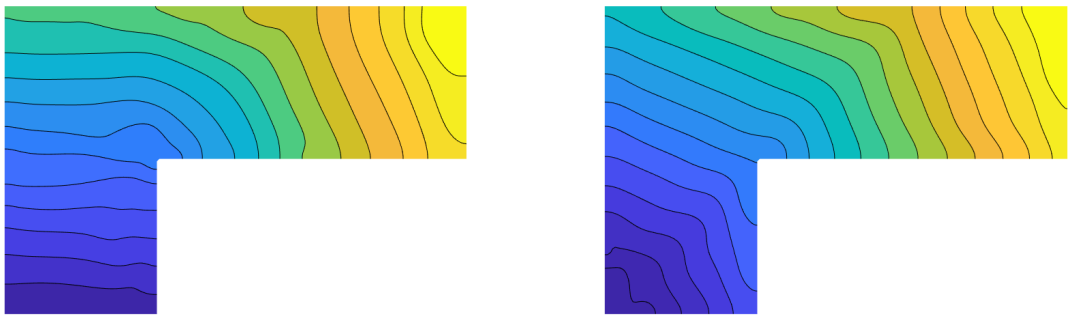

(a) Obj: distortion = 3.0E-3 **(b)** Obj: distortion = 7.7E-3

Figure 3.6: Optimized fabrication sequences to minimize distortion with layer thickness control for two different initial time fields

Figure 3.7 shows that the optimization converges within the 500 iterations. The objective converges quickly at the start and slowly reduces further. The speed of the convergence is dependent on the weight attributed to the uniform thickness objective and the imposed constraints that need to be satisfied. The rate of convergence can further be increased by increasing the maximum step size of the design variables used by MMA. This however can result in local minima and maxima in the time field which can then have a negative effect on the convergence rate.

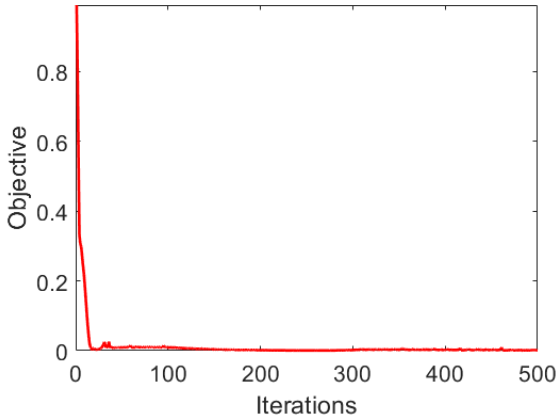

Figure 3.7: Convergence plot of the objective function

In Figure 3.8a the volumes of the layers are shown as a fraction of the total volume of the part. In previous work the time points T_p were fixed and thus the volumes of the layers were fixed to ensure constant fabrication speed. With the modified fabrication speed constraint shown in Equation 3.10 the layers can now vary in volume. In Figure 3.8b the normalized fabrication speeds are shown for the layers. The fabricated elements per unit time are divided by the number of elements of the part that are fabricated within the pseudo-time range $t_e \in [0, 1]$. The figure shows similar fabrication speeds of the layers with small variations. This means that the constant fabrication speed is maintained with varying time points T_p.

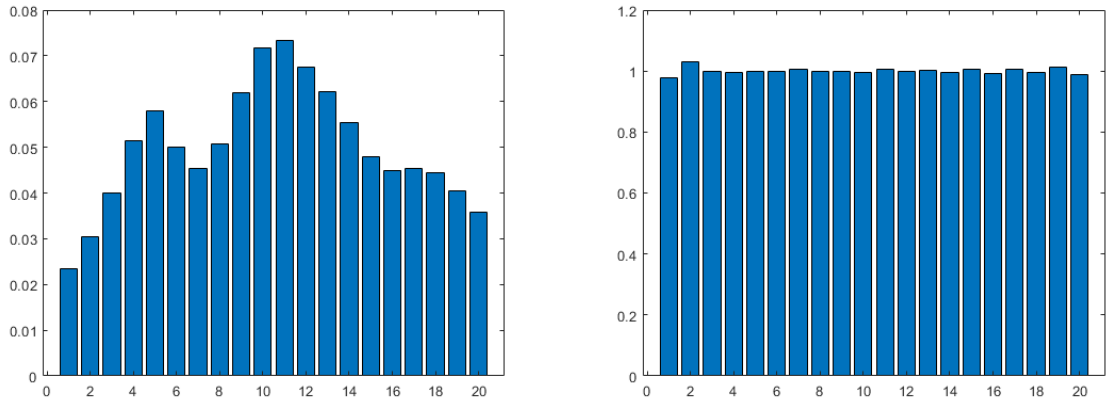

(a) Volumes of the layers as a fraction of the total volume

(b) Normalized fabrication speed of the layers

Figure 3.8: Effect of the modified constraint to ensure constant fabrication speed

As the thickness constraint is determined by fabrication equipment characteristics it is important that the thickness computed from the gradient magnitude is accurate enough. To get a measure for the accuracy, the thicknesses calculated from the gradient magnitudes are compared to the geometrically calculated thicknesses. Here, the geometrical thickness is evaluated by taking the average normal distance of the upper and lower boundaries of the layer. In Figure 3.9 the thicknesses for both calculations. It can be seen that the gradient calculated thicknesses are mostly consistent with the geometrical thicknesses. Some of the variations can be attributed to the boundaries of the part.

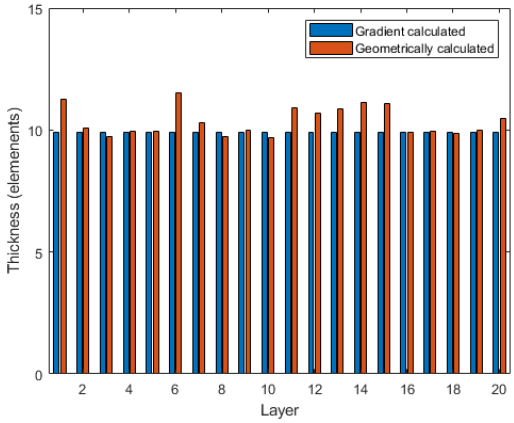

Figure 3.9: Thicknesses of the layers computed from gradients and geometric boundaries

3.4.2. Parameter study

A parameter study was done to show the influence of the weight factor of the uniform thickness objective on the optimization results. The weight factor determines the importance of the uniform thickness objective in the optimization relative to the distortion minimization. The study was done by varying the weight factor and comparing the optimization results to the original without layer thickness control. The results of the parameter study showed that the weight factor has a significant impact on the optimization results. A higher weight factor leads to more uniform layer thickness, but also to a higher distortion. A lower weight factor leads to less uniform layer thickness, but also to a lower distortion. The optimal weight factor depends on the specific application and the desired trade-off between uniform layer thickness and distortion. In Figure 3.10c it can be seen that the varying weight factors show little effect on the shape of the layers. This is because the time field that is used to initialize the building direction is closer to the optimal sequence to minimize distortion and the effect that the thickness constraint in Equation 3.12 already has on the thickness of the layers. Increasing the weight factor does however

still influence the propagation of the time values within each layer. As can be seen from the distortion values, increasing the weight factor does lead to an increasement in the distortion.

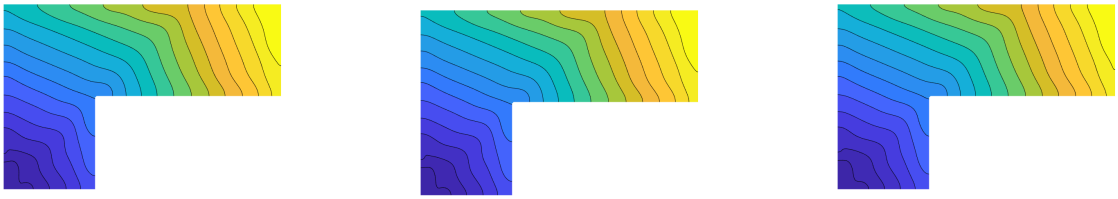

(a) Obj: distortion = 2.27E-3 weight: 0.01

(b) Obj: distortion = 7.69E-3 weight: 1

(c) Obj: distortion = 5.4E-2 weight: 1000

Figure 3.10: Layer thickness controlled optimization with the initial time field starting from the bottom left

When the initial time field is changed to start from the building plate, the effects of the varying weights become more clear. For higher weight factors the optimizations show more uniform layer thickness as can be seen in Figure 3.11c.

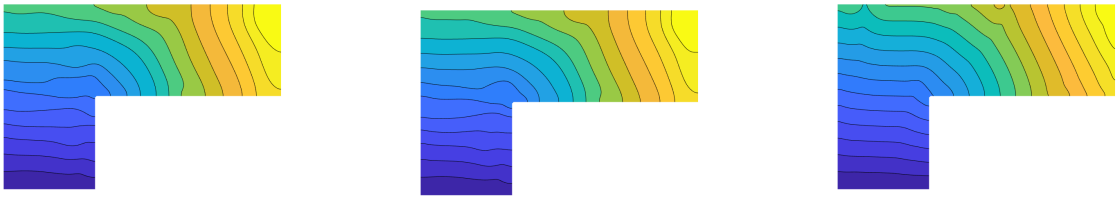

(a) Obj: distortion = 1.0E-2 weight: 0.01

(b) Obj: distortion = 3.06E-2 weight: 1

(c) Obj: distortion = 1.5 weight: 1000

Figure 3.11: Layer thickness controlled optimization with the initial time field starting from the bottom

In Figure 3.12a and Figure 3.12b the effect of the weights on the gradient magnitudes of the time field are shown. It can be seen that the increased weight factor causes the magnitudes to become more constant which then results in the more uniform layer thickness.

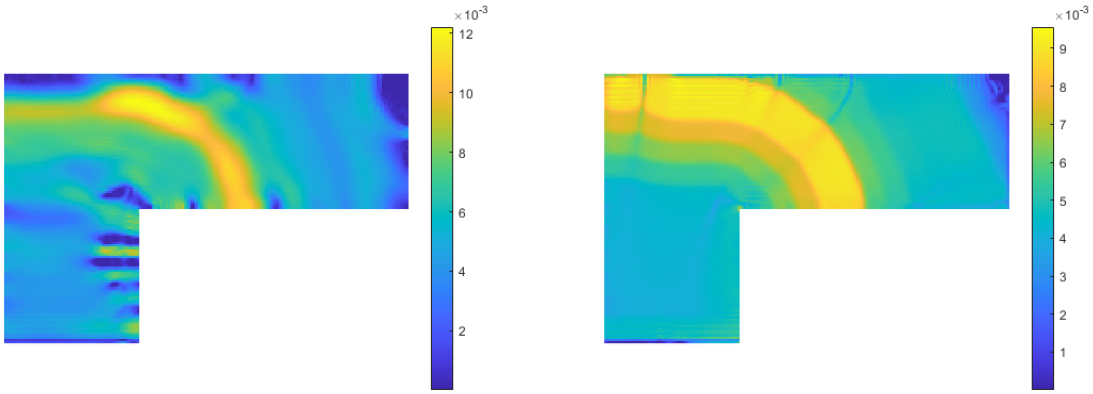

(a) Gradient magnitudes for weight: 1

(b) Gradient magnitudes for weight: 1000

Figure 3.12: Effect of the weighting factor on the gradient magnitude field

To show the effect of the weight factor on both the distortion and the thickness variation two graphs are shown in Figure 3.13a and Figure 3.13b. The distortion is measured by taking the average displace-

ments of the nodes of interest. To get a measure for the thickness uniformity, the coefficient of variation, also known as the relative standard deviation, is used. The formula for the coefficient of variation is shown in Equation 3.36.

$$CV_j = \frac{\sigma_j}{\mu_j}, \qquad j = 1, ..., N, \tag{3.36}$$

$$\sigma_j = \sqrt{\frac{\sum \left(M^j - m_t^j\right)^2}{V_j}} \tag{3.37}$$

$$\mu_j = m_t^j \tag{3.38}$$

The graphs clearly show the trade-off between distortion optimization and uniform thickness. Depending on the fabrication equipment a weight factor can be chose such that the variation in layer thickness is within the limits of the equipment.

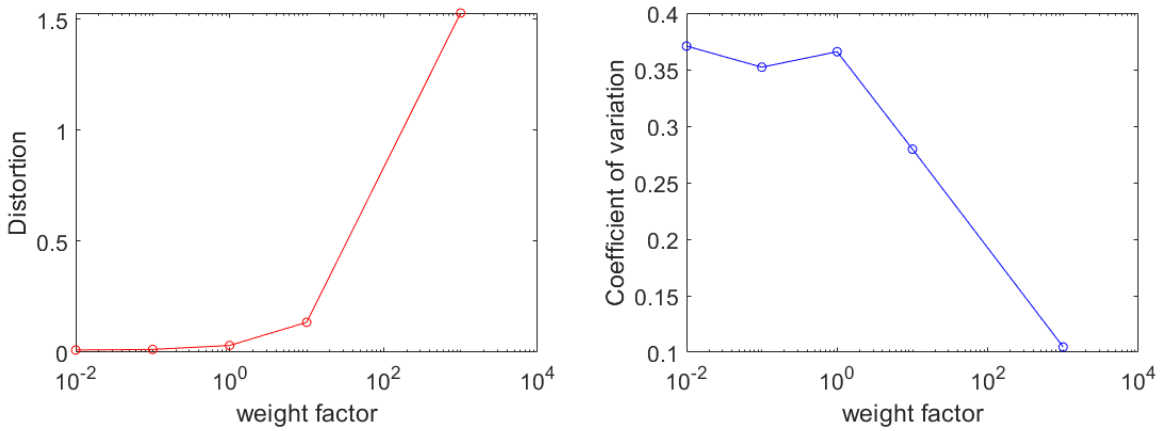

(a) Distortion values for varying weight factors

(b) Coefficients of variance for varying weight factors

Figure 3.13: Effect of the weight factor on the distortion and variance in gradient magnitude

3.4.3. 2D Bracket

To show the effect of the layer thickness control, the optimization was done for several 2D shapes. The second example is a 2D bracket, shown in Equation 3.39. The domain is discretized by a finite element grid of 144 x 96. The fabrication is supposed to start from the corner on the bottom left or the entire bottom of the part as shown in Figure 3.14c and Figure 3.14b. The nodes on the bottom of the component are fixed in the process simulation. The number of layers is set to 12. The distortion is measured by the average of the displacements of nodes on the inner circle (red) as shown in Figure 3.14a by using the following formulation

$$d = \frac{1}{n\left(\mathcal{W}\right)} \sum_{j \in \mathcal{W}} \left(\left(u_j^x\right)^2 + \left(u_j^y\right)^2\right) \tag{3.39}$$

where $\mathcal{W}$ is the set of nodes along the circle and d is defined as the average displacement of the nodes on the inner circle.

(a) Given component **(b)** Initial time field from the bottom left **(c)** Initial time field from the bottom

Figure 3.14: Initialization of the 2D bracket

In Figure 3.15a and Figure 3.15b the results of the distortion minimization without layer control can be seen. In Figure 3.15c and Figure 3.15d the results from the thickness controlled optimization are shown. The optimizations starting from the bottom show small differences in the shape of the layers. This is due to the fact the optimization of the part can mostly be done in planar layers when building in the given direction. For the optimizations starting from the bottom left the differences become more clear. The thickness controlled optimization shows a more constant thickness of the layers and less variation over the length of the layer. Some variation in the thickness of the layers can still be seen. This is due to the initialized building direction in combination with the limited number of layers N for the complexity of the part. The measured distortion values show a clear increase due to the thickness control method. This is expected as the manufacturability is now accounted for which decreases the design freedom of the optimization.

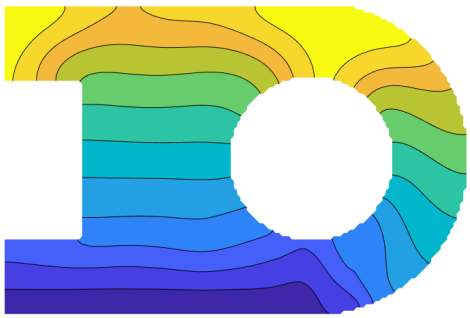

(a) Original optimization for minimizing distortion
Obj: distortion = 8E-5

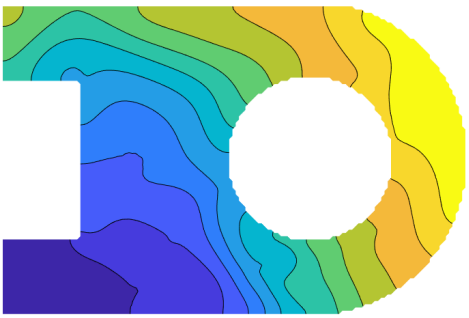

(b) Layer controlled optimization
Obj: distortion = 9E-5

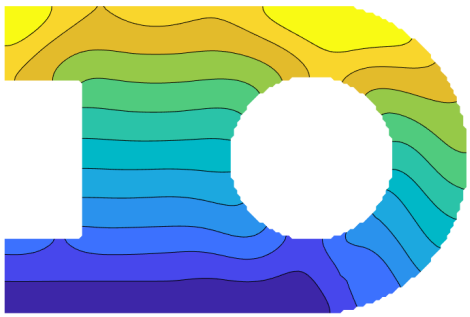

(c) Original optimization for minimizing distortion
Obj: distortion = 5E-4

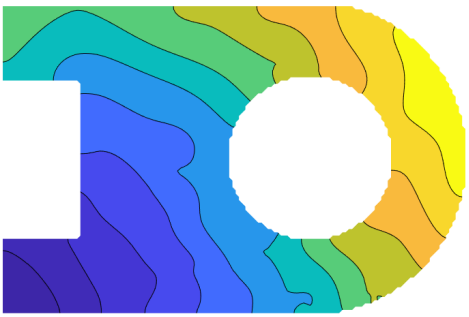

(d) Layer controlled optimization
Obj: distortion = 7.3E-3

Figure 3.15: Effect of the layer thickness control on the 2D bracket for two differnent initial time fields

4

Discussion and conclusions

4.1. Conclusions

In this thesis, we have presented a method to control the layer thickness in fabrication sequence optimization. The method makes use of the gradient magnitudes computed from the pseudo-time field to control the variation in the objective function. Numerical results show that the method is effective in controlling the absolute value of the layer thickness as well as the variation of the thickness over the length of the layer. To test the method, the framework for minimizing distortion was used. As expected, the improvement in manufacturability in the optimized fabrication sequence restricted the freedom to optimize for minimal distortion. By adjusting the weight factor and the thickness target for the constraint, one can control the nominal thickness and thickness variation of the layers.

4.2. Shortcomings of the layer thickness control method

The results in this thesis in chapter 3 show the effectiveness of the layer thickness control method in fabrication sequence optimization. The layers are more uniform in thickness when the control method is applied. Although the method is generally applicable to sequence optimizations including a time field, its effect in STTO can be less apparent. This is due to the varying density field that can result in thin geometries smaller than the target thickness of the layers.

4.3. Future work

The work presented in this thesis forms a first step in controlling the layer thickness in fabrication sequence optimized designs. Further steps can be taken to improve the manufacturability of fabrication sequence optimized designs. In this section some directions of future work are suggested.

4.3.1. Extension to 3D

The layer thickness control method can be extended to 3D by including the gradients in the z-direction to the gradient magnitude computation as shown in Equation 4.1. The objective and constraint formulations are based on this gradient magnitude and will have the same effect as in 2D.

$$M = \|\nabla T\| = \sqrt{\left(\frac{dt}{dx}\right)^2 + \left(\frac{dt}{dy}\right)^2 + \left(\frac{dt}{dz}\right)^2} \tag{4.1}$$

With the extension to 3D a new challenge arises for the tool path planning. The 3D curved layer can require multiple tool passes to fabricate and thus controlling the width of the layer offers a new challenge in the fabrication sequence optimization process. Currently the layer is assumed to be fabricated at once. Ideally however, the optimization would also consider the toolpath within each layer.

4.3.2. Extension to STTO

Although the proposed method is efffective in controlling the thickness of the time field of the optimization, it does not guarantee uniform thickness in STTO. Due to the variable density field, voids within

the projected layer can cause varying layer thickness in these optimized fabrication sequences. This variation in layer thickness can be seen in Figure 4.1.

Figure 4.1: Layers of the STTO design

A possible method to tackle this problem is to use discrete object projection [3] within each layer to ensure length scale control on the voids and solids between the isolines of the time field. A visualization of the discrete projection using a prescribed object is shown in Figure 4.2.

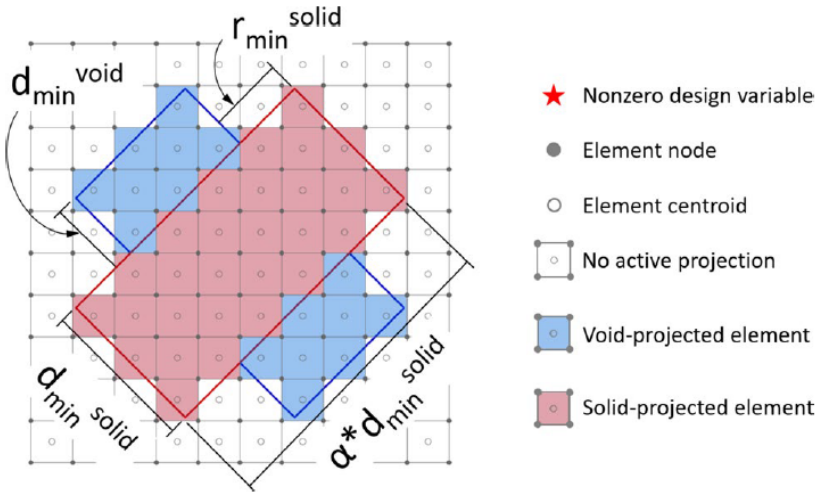

Figure 4.2: Discrete object projection using a bead primitive [3]

When these bead primitives are oriented in the shape of the isolines of the time field the elements of a layer within that bead primitive will be projected to either void or solid. In Figure 4.3 a curved layer is shown using multiple bead primitives in different orientations. This could help solving the variable layer thickness in STTO designs due to the varying density field.

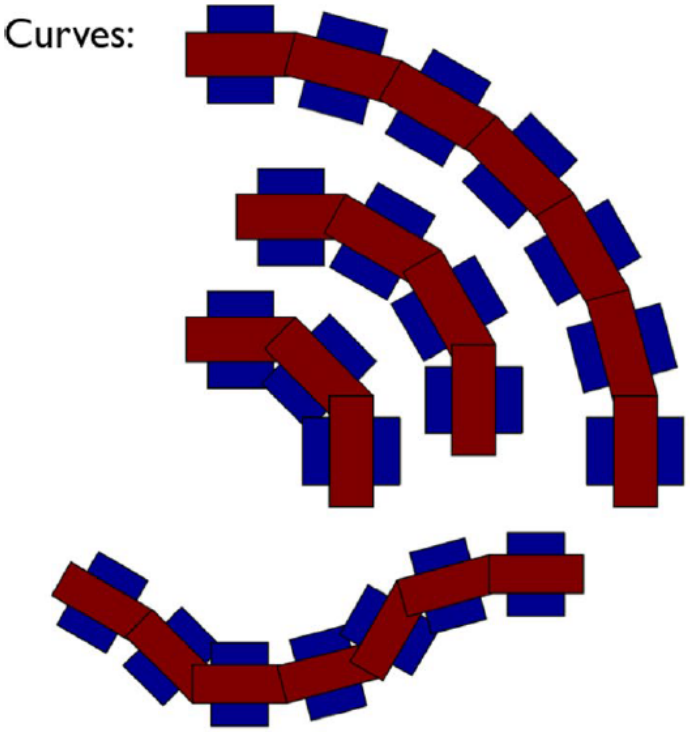

Figure 4.3: Curved layer using bead primitives [3]

Other length scale control methods such as the robust formulations [30] can be applied to ensure minimum feature size on the void and solid phase. This can reduce the variation in layer thickness due to optimized material distribution.

4.3.3. Number of layers

The number of layers used for the optimization process is a prescribed parameter in this work. It can be selected by

$$N = \frac{h}{\bar{d}} \tag{4.2}$$

where h is the height of the part in the initial building direction and $\bar{d}$ is desired the nominal thickness of the layers dependent of the additive manufacturing equipment characteristics. This formulation offers a good estimate of the required layers to fabricate the given component but could limit the freedom in layer dimensions and orientation. Possible future work could include making the number of layers N a design variable, where the number of layers can go up or down to satisfy the layer thickness constraints.

References

[1] Oded Amir and Yoram Mass. “Topology optimization for staged construction”. In: *Structural and Multidisciplinary Optimization* 57.4 (2018), pp. 1679–1694.

[2] M. Bruyneel and P. Duysinx. “Note on topology optimization of continuum structures including self-weight”. In: *Structural and Multidisciplinary Optimization* 29.4 (2005), pp. 245–256.

[3] Julia D. Carroll and James K. Guest. “Topology optimization of uniform thickness structures using discrete object projection”. In: *Structural and Multidisciplinary Optimization* 65.9 (2022), pp. 1–16.

[4] Keenan Crane, Clarisse Weischedel, and Max Wardetzky. “The heat method for distance computation”. In: *Communications of the ACM* 60.11 (2017), pp. 90–99.

[5] Chengkai Dai, Charlie C.L. Wang, Chenming Wu, Sylvain Lefebvre, Guoxin Fang, and Yong Jin Liu. “Support-free volume printing by multi-axis motion”. In: *ACM Transactions on Graphics* 37.4 (2018).

[6] Guoxin Fang, Tianyu Zhang, Sikai Zhong, Xiangjia Chen, Zichun Zhong, and Charlie C.L. Wang. “Reinforced FDM: Multi-axis filament alignment with controlled anisotropic strength”. In: *ACM Transactions on Graphics* 39.6 (2020).

[7] J. K. Guest, J. H. Prévost, and T. Belytschko. “Achieving minimum length scale in topology optimization using nodal design variables and projection functions”. In: *International Journal for Numerical Methods in Engineering* 61.2 (2004), pp. 238–254.

[8] Linus Hägg and Eddie Wadbro. “On minimum length scale control in density based topology optimization”. In: *Structural and Multidisciplinary Optimization* 58.3 (2018), pp. 1015–1032.

[9] Kristian Hildebrand, Bernd Bickel, and Marc Alexa. “Orthogonal slicing for additive manufacturing”. In: *Computers and Graphics (Pergamon)* 37.6 (2013), pp. 669–675.

[10] Rameez Israr, Johannes Buhl, and Markus Bambach. “A study on power-controlled wire-arc additive manufacturing using a data-driven surrogate model”. In: *International Journal of Advanced Manufacturing Technology* 117.7-8 (2021), pp. 2133–2147.

[11] Davoud Jafari, Tom H.J. Vaneker, and Ian Gibson. “Wire and arc additive manufacturing: Opportunities and challenges to control the quality and accuracy of manufactured parts”. In: *Materials and Design* 202 (2021).

[12] Nam H Kim. “Chapter 4 Sensitivity Analysis”. In: December 2010 (2017).

[13] Weixian Lan and United States. “Efficient Layer-by-Layer Simulation for Topology Optimization”. In: (2022).

[14] Jikai Liu, Andrew T. Gaynor, Shikui Chen, Zhan Kang, Krishnan Suresh, Akihiro Takezawa, Lei Li, Junji Kato, Jinyuan Tang, Charlie C.L. Wang, Lin Cheng, Xuan Liang, and Albert C. To. “Current and future trends in topology optimization for additive manufacturing”. In: *Structural and Multidisciplinary Optimization* 57.6 (2018), pp. 2457–2483.

[15] Comput Methods, Appl Mech, G A Haveroth, C Thore, M R Correa, R F Ausas, S Jakobsson, and J A Cuminato. “ScienceDirect Topology optimization including a model of the layer-by-layer additive manufacturing process”. In: 398 (2022).

[16] Grzegorz Misiun, Emiel van de Ven, Matthijs Langelaar, Hubert Geijselaers, Fred van Keulen, Ton van den Boogaard, and Can Ayas. “Topology Optimization for additive manufacturing with distortion constraints”. In: *Computer Methods in Applied Mechanics and Engineering* 386 (2021), p. 114095.

[17] Helena Monteiro, Gabriel Carmona-Aparicio, Inês Lei, and Mélanie Despeisse. “Energy and material efficiency strategies enabled by metal additive manufacturing – A review for the aeronautic and aerospace sectors”. In: *Energy Reports* 8 (2022), pp. 298–305.

[18] M. P. Mughal, R. A. Mufti, and H. Fawad. “The mechanical effects of deposition patterns in welding-bflsed layered manufacturing”. In: *Proceedings of the Institution of Mechanical Engineers, Part B: Journal of Engineering Manufacture* 221.10 (2007), pp. 1499–1509.

[19] S M E North, Isothermal Surface, Yujie Shan, and Dongming Gan. “ScienceDirect ScienceDirect ScienceDirect Curved Layer Layer Slicing Slicing based based on on Isothermal Surface Curved Curved Layer Slicing based on Isothermal Surface”. In: *Procedia Manufacturing* 53 (2021), pp. 484–491.

[20] Jesús Emilio Pinto-Lopera, José Mauricio S.T. Motta, and Sadek Crisostomo Absi Alfaro. “Real-time measurement of width and height of weld beads in GMAW processes”. In: *Sensors (Switzerland)* 16.9 (2016), pp. 1–14.

[21] Tiago A. Rodrigues, V. Duarte, R. M. Miranda, Telmo G. Santos, and J. P. Oliveira. “Current status and perspectives on wire and arc additive manufacturing (WAAM)”. In: *Materials* 12.7 (2019).

[22] Ole Sigmund and Kurt Maute. “Topology optimization approaches: A comparative review”. In: *Structural and Multidisciplinary Optimization* 48.6 (2013), pp. 1031–1055.

[23] Sagar Singh, Satish Kumar Sharma, and Dinesh W. Rathod. “A review on process planning strategies and challenges of WAAM”. In: *Materials Today: Proceedings* 47 (2020), pp. 6564–6575.

[24] John C. Steuben, Athanasios P. Lliopoulos, and John G. Michopoulos. “Towards multiscale topology optimization for additively manufactured components using implicit slicing”. In: *Proceedings of the ASME Design Engineering Technical Conference* 1.October 2018 (2017).

[25] Krister Svanberg. “The method of moving asymptotes—a new method for structural optimization”. In: *International Journal for Numerical Methods in Engineering* 24.2 (1987), pp. 359–373.

[26] Jumyung Um, Joungmin Park, and Ian Anthony Stroud. “applied sciences Squashed-Slice Algorithm Based on STEP-NC for Multi-Material and Multi-Directional Additive Processes”. In: (2021).

[27] Emiel van de Ven, Robert Maas, Can Ayas, Matthijs Langelaar, and Fred van Keulen. “Overhang control in topology optimization: a comparison of continuous front propagation-based and discrete layer-by-layer overhang control”. In: *Structural and Multidisciplinary Optimization* 64.2 (2021), pp. 761–778.

[28] K. E.K. Vimal, M. Naveen Srinivas, and Sonu Rajak. “Wire arc additive manufacturing of aluminium alloys: A review”. In: *Materials Today: Proceedings* 41 (2019), pp. 1139–1145.

[29] Chao Wang, Bin Xu, Zunyi Duan, and Jianhua Rong. “Structural topology optimization considering both manufacturability and manufacturing uncertainties”. In: *Structural and Multidisciplinary Optimization* 66.1 (2023), pp. 1–18.

[30] Fengwen Wang, Boyan Stefanov Lazarov, and Ole Sigmund. “On projection methods, convergence and robust formulations in topology optimization”. In: *Structural and Multidisciplinary Optimization* 43.6 (2011), pp. 767–784.

[31] Weiming Wang, Fred Keulen, and Jun Wu. “Fabrication Sequence Optimization for Minimizing Distortion in Multi-Axis Additive Manufacturing”. In: *Additive Manufacturing* (2022).

[32] Weiming Wang, Dirk Munro, Charlie C.L. Wang, Fred van Keulen, and Jun Wu. “Space-time topology optimization for additive manufacturing: Concurrent optimization of structural layout and fabrication sequence”. In: *Structural and Multidisciplinary Optimization* 61.1 (2020), pp. 1–18.

[33] S. W. Williams, F. Martina, A. C. Addison, J. Ding, G. Pardal, and P. Colegrove. “Wire + Arc additive manufacturing”. In: *Materials Science and Technology (United Kingdom)* 32.7 (2016), pp. 641–647.

[34] Kaufui V. Wong and Aldo Hernandez. “A Review of Additive Manufacturing”. In: *ISRN Mechanical Engineering* 2012 (2012), pp. 1–10.

[35] Jing Xu, Xizhi Gu, Donghong Ding, Zengxi Pan, and Ken Chen. “A review of slicing methods for directed energy deposition based additive manufacturing”. In: *Rapid Prototyping Journal* 24.6 (2018), pp. 1012–1025.

[36] Tomás Zegard and Glaucio H. Paulino. “Bridging topology optimization and additive manufacturing”. In: *Structural and Multidisciplinary Optimization* 53.1 (2016), pp. 175–192.

[37] Mingdong Zhou, Boyan S. Lazarov, Fengwen Wang, and Ole Sigmund. “Minimum length scale in topology optimization by geometric constraints”. In: *Computer Methods in Applied Mechanics and Engineering* 293 (2015), pp. 266–282.

[38] Jihong ZHU, Han ZHOU, Chuang WANG, Lu ZHOU, Shangqin YUAN, and Weihong ZHANG. “A review of topology optimization for additive manufacturing: Status and challenges”. In: *Chinese Journal of Aeronautics* 34.1 (2021), pp. 91–110.

A

Appendix A

A.1. Time projection of a layer

The functions $ft(t, tP)$ and $gt(t, tP)$ are used to isolate the elements of a specific layer. Here ft is the threshold projection using the upper time point and gt is the threshold projection using the lower time point. By substracting the two we can isolate the layer between its time points $tP(i)$ and $tP(i+1)$. In A.1

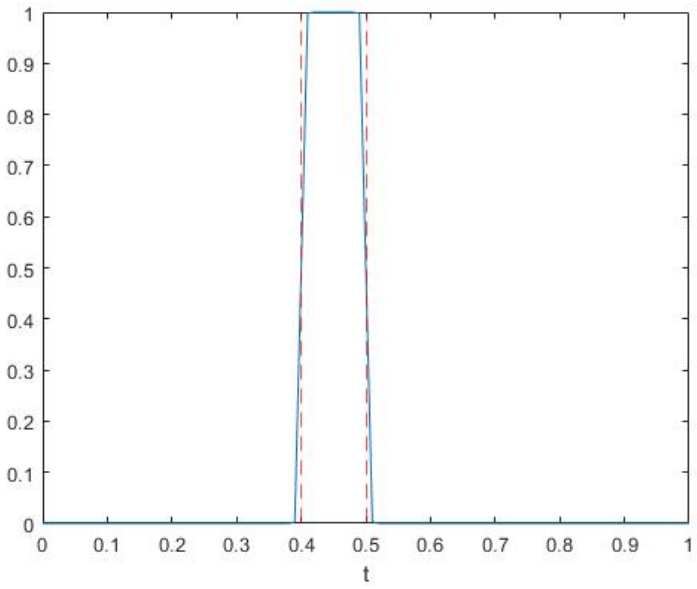

Figure A.1: Function to isolate the element values of a specific layer to use in constraints or objectives

B

Appendix B

B.1. Finite Difference sensitivity check

The objective and constraint functions are functions of the design variables t, T_p. The sensitivities are computed by taking the derivative of these functions with respect to the design variables. To make sure the sensitivities are computed correctly, a Finite Difference check can be done to compare the values of the obtained derivatives. In the following sections the Finite Difference checks are plotted for the design variables. The design variables are perturbed as shown in Equation B.1 and Equation B.3.

$$t_i = t_i + \Delta t \tag{B.1}$$

$$\Delta t = 10^{-j}, \qquad j = 1, 2, ..., 9 \tag{B.2}$$

$$T_p = T_p + \Delta T_p \tag{B.3}$$

$$\Delta T_p = 10^{-j}, \qquad j = 1, 2, ..., 9 \tag{B.4}$$

B.1.1. Objective function sensitivities

The objective function displays the performance of the optimized fabrication sequence on the distortion and the uniform thickness. The Finite difference check is done using Equation B.5. The objective function depends on the design variables t and T_p for which the Finite Difference checks are plotted in Figure B.1 and Figure B.2 respectively.

$$S_{obj}(t) = \left| \frac{FD_{obj}(t_i + \Delta t)}{\frac{\partial obj(t_i)}{\partial t}} - 1 \right| \tag{B.5}$$

$$S_{obj}(T_p) = \left| \frac{FD_{obj}(T_p + \Delta T_p)}{\frac{\partial obj(T_p)}{\partial T_p}} - 1 \right| \tag{B.6}$$

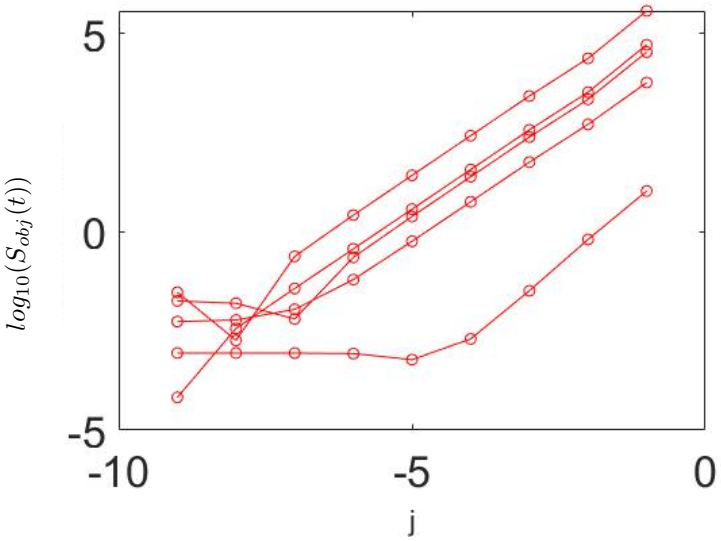

Figure B.1: Finite difference check of the objective w.r.t time value on the nodes t

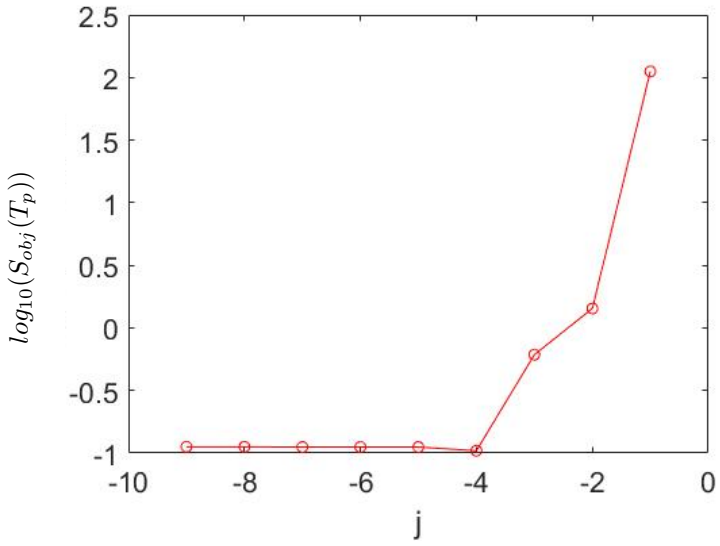

Figure B.2: Finite difference check of the objective w.r.t the time point T_p

B.1.2. Constraint sensitivities

There are several constraints applied in the optimization model. In the following sections the finite difference curves of the constraints w.r.t the design variables are plotted to confirm the accuracy of the derivatives of the functions. The Finite difference check is done using Equation B.5.

$$S_{cons}(t) = \left| \frac{FD_{cons}(t_i + \Delta t)}{\frac{\partial cons(t_i)}{\partial t}} - 1 \right| \tag{B.7}$$

$$S_{cons}(T_p) = \left| \frac{FD_{cons}(T_p + \Delta T_p)}{\frac{\partial cons(T_p)}{\partial T_p}} - 1 \right| \tag{B.8}$$

Minimum volume constraint

The minimum volume constraint bounds the lower limit of the volume of each layer. The constraint function depends on the design variables t and T_p for which the Finite Difference checks are plotted in Figure B.3 and Figure B.4 respectively.

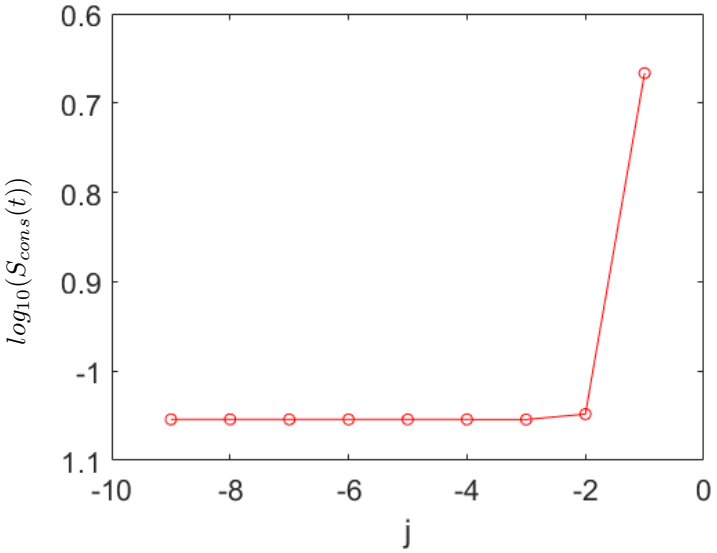

Figure B.3: Finite difference check of the minimum volume constraint w.r.t the time value on the nodes t

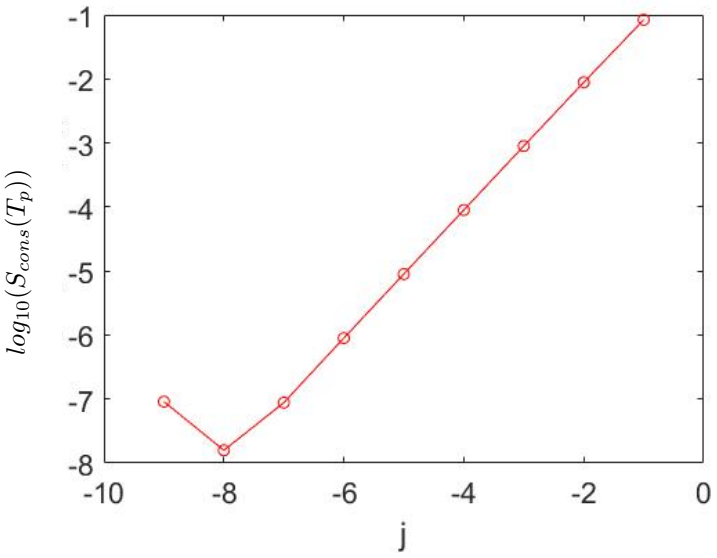

Figure B.4: Finite difference check of the minimum volume constraint w.r.t the time point T_p

Constant fabrication speed constraint

The fabrication speed constraint bounds the lower and upper limit of the deposited volume at each time point to ensure constant fabrication speed. The constraint function depends on the design variables t and T_p for which the Finite Difference checks are plotted in Figure B.5 and Figure B.6 respectively.

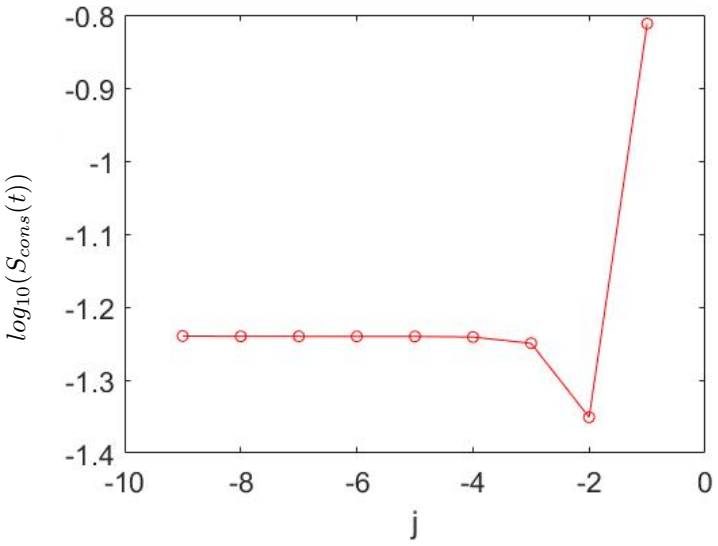

Figure B.5: Finite difference check of the fabrication speed constraint w.r.t the time value on the nodes t

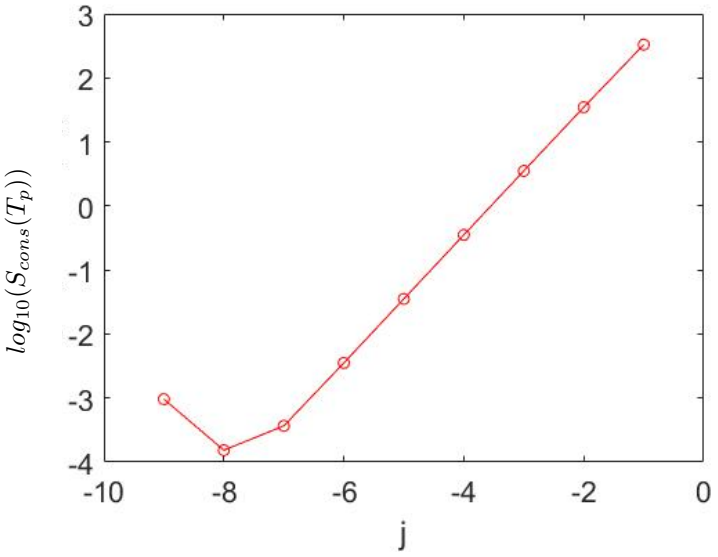

Figure B.6: Finite difference check of the fabrication speed constraint w.r.t the time point T_p

Thickness constraint

The thickness constraint bounds the lower and upper limit of the thickness of each layer. The constraint function depends on the design variables t and T_p for which the Finite Difference checks are plotted in Figure B.7 and Figure B.8 respectively.

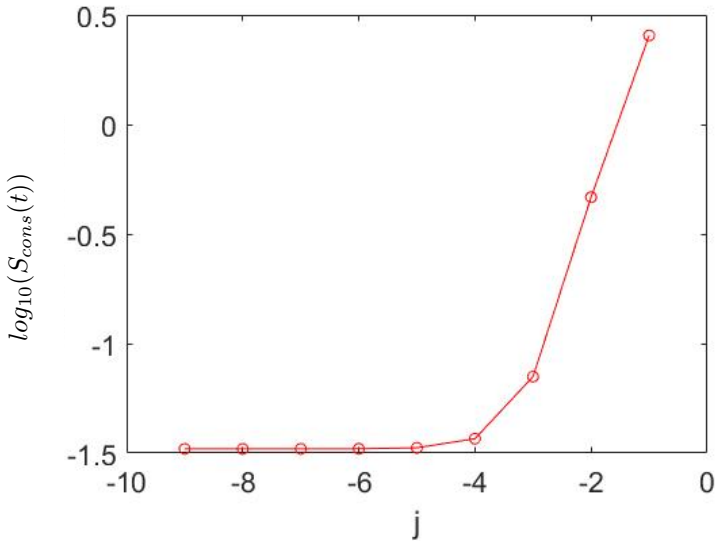

Figure B.7: Finite difference check of the thickness constraint w.r.t the time value on the nodes t

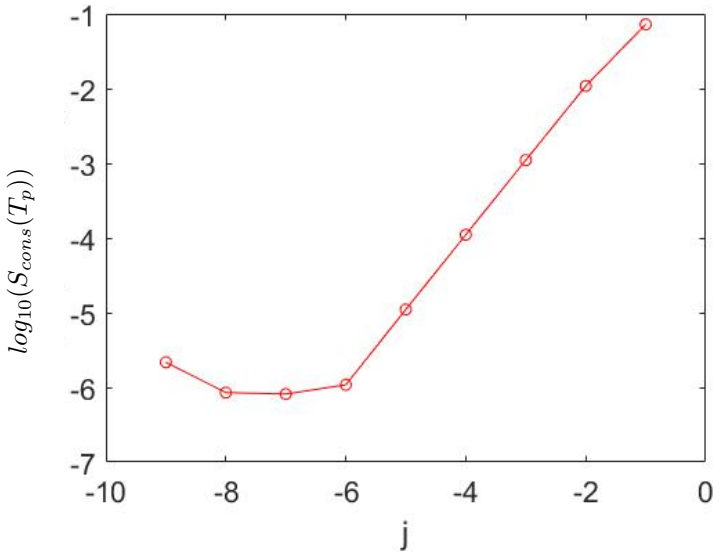

Figure B.8: Finite difference check of the thickness constraint w.r.t the time point T_p

Appendix C

C.1. Local minima

The proposed method to control the variation of the thickness of the layers uses the magnitude of the gradients of the elements. This way only the absolute value is controlled and not the direction of the gradient magnitude. This therefore can not guarantee an optimized time field free from local minima. In Figure C.1a and Figure C.1b the gradients are shown. The occurrence of these local minima can be

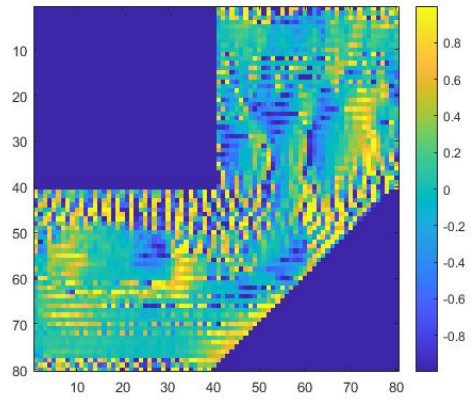

(a) Gradients of the elements in x-direction

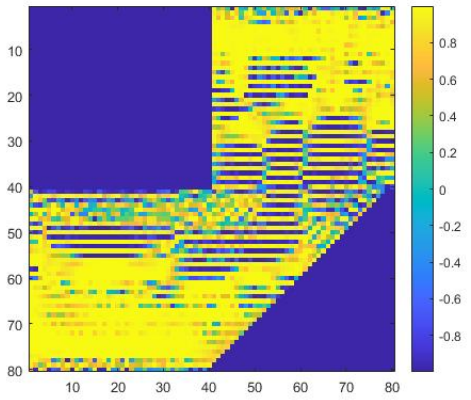

(b) Gradients of the elements in y-direction

reduced by using the continuity filter and by reducing the maximum step-size of the design variables per iteration. This results in a more positive gradient field for the y-direction as shown in Figure C.2.

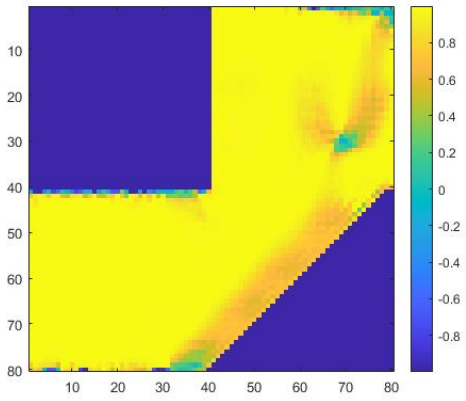

Figure C.2: Gradient in y-direction with reduced local minima